The Astrophysical Journal, 568:845–861, 2002 April 1

DYNAMICAL EVIDENCE FOR A BLACK HOLE IN THE MICROQUASAR XTE J1550−564[1]

Jerome A. Orosz
Astronomical Institute, Utrecht University, Postbus 80000, 3508 TA Utrecht, Netherlands; J.A.Orosz@astro.uu.nl

Paul J. Groot
Harvard-Smithsonian Center for Astrophysics, 60 Garden Street, Cambridge, MA 02138; pgroot@cfa.harvard.edu

Michiel van der Klis
Astronomical Institute "Anton Pannekoek," University of Amsterdam, and Center for High-Energy Astrophysics, Kruislaan 403, 1098 SJ Amsterdam, Netherlands; michiel@astro.uva.nl

Jeffrey E. McClintock, Michael R. Garcia, and Ping Zhao
Harvard-Smithsonian Center for Astrophysics, 60 Garden Street, Cambridge, MA 02138; jem@cfa.harvard.edu, garcia@cfa.harvard.edu, zhao@cfa.harvard.edu

Raj K. Jain
Department of Physics, Yale University, P.O. Box 208120, New Haven, CT 06520-8120; rjain@astro.yale.edu

Charles D. Bailyn
Department of Astronomy, Yale University, P.O. Box 208101, New Haven, CT 06520-8101; bailyn@astro.yale.edu

and

Ronald A. Remillard
Center for Space Research, Massachusetts Institute of Technology, Cambridge, MA 02139-4307; rr@space.mit.edu
Received 2001 August 15; accepted 2001 December 5

ABSTRACT

Optical spectroscopic observations of the companion star (type G8 IV to K4 III) in the microquasar system XTE J1550−564 reveal a radial velocity curve with a best-fitting spectroscopic period of $P_{\rm sp} = 1.552 \pm 0.010$ days and a semiamplitude of $K_2 = 349 \pm 12$ km s^{-1}. The optical mass function is $f(M) = 6.86 \pm 0.71\ M_\odot$ (1 σ). We tentatively measure the rotational velocity of the companion star to be $V_{\rm rot} \sin i = 90 \pm 10$ km s^{-1}, which when taken at face value implies a mass ratio of $Q \equiv M_1/M_2 = 6.6^{+2.5}_{-1.6}$ (1 σ), using the above value of K_2. We derive constraints on the binary parameters from simultaneous modeling of the ellipsoidal light and radial velocity curves. We find 1 σ ranges for the photometric period (1.5430 days $\leq P_{\rm ph} \leq$ 1.5440 days), K-velocity ($350.2 \leq K_2 \leq 368.6$ km s^{-1}), inclination ($67\overset{\circ}{.}0 \leq i \leq 77\overset{\circ}{.}4$), mass ratio ($Q \geq 12.0$), and orbital separation ($11.55\ R_\odot \leq a \leq 12.50\ R_\odot$). Given these geometrical constraints, we find that the most likely value of the mass of the compact object is 9.41 $M_\odot$ with a 1 σ range of $8.36\ M_\odot \leq M_1 \leq 10.76\ M_\odot$. If we apply our tentative value of $V_{\rm rot} \sin i = 90 \pm 10$ km s^{-1} as an additional constraint in the ellipsoidal modeling, we find 1 σ ranges of 1.5432 days $\leq P_{\rm ph} \leq$ 1.5441 days for the photometric period, $352.2 \leq K_2 \leq 370.1$ km s^{-1} for the K-velocity, $70\overset{\circ}{.}8 \leq i \leq 75\overset{\circ}{.}4$ for the inclination, $6.7 \leq Q \leq 11.0$ for the mass ratio, and $12.35\ R_\odot \leq a \leq 13.22\ R_\odot$ for the orbital separation. These geometrical constraints imply the most likely value of the mass of the compact object of 10.56 $M_\odot$ with a 1 σ range of $9.68\ M_\odot \leq M_1 \leq 11.58\ M_\odot$. In either case the mass of the compact object is well above the maximum mass of a stable neutron star, and we therefore conclude that XTE J1550−564 contains a black hole.

Subject headings: binaries: spectroscopic — black hole physics — stars: individual (XTE J1550−564) — X-rays: binaries — X-rays: stars

1. INTRODUCTION

X-ray novae provide the strongest evidence for the existence of stellar mass black holes. These objects are interacting binaries containing a compact primary (a neutron star or a black hole) and what is usually a late-type secondary. X-ray novae spend most of their time in a low X-ray luminosity "quiescent" state, with an X-ray luminosity ($L_{\rm X}$) roughly similar to the optical luminosity ($L_{\rm opt}$), which includes a substantial contribution from the secondary star ($L_{\rm star}$). The quiescent state is occasionally interrupted by "outbursts" where typically $L_{\rm X} \gg L_{\rm opt} \gg L_{\rm star}$. In quiescence, the observed radial velocity and light curves of the secondary star lead to dynamical mass estimates for the compact primary. If its mass exceeds the maximum stable mass of a neutron star ($\approx 3\ M_\odot$), the compact object is presumed to be a black hole (Chitre & Hartle 1976; Kalogera & Baym 1996). In 13 cases the mass of the primary of an X-ray nova has been shown to exceed 3 $M_\odot$, confirming the presence of black holes in these systems (Bailyn et al. 1995; Casares, Charles, & Naylor 1992; Casares, Charles, & Marsh 1995; Filippenko, Matheson, & Ho 1995; Filippenko et al. 1999; Filippenko & Chornock 2001; Greiner, Cuby, & McCaughrean 2001; McClintock & Remillard 1986; McClintock et al. 2001; Orosz et al. 1998b, 2001; Remillard, McClintock, & Bailyn 1992; Remillard et al. 1996). These X-ray novae open up the possibility of studying the strong-

[1] Based on observations collected at the European Southern Observatory, Chile (program 67.D-0229), at the Magellan Walter Baade Telescope at the Las Campanas Observatory, Chile, and the William Herschel Telescope operated on the island of La Palma by the Isaac Newton Group in the Spanish Observatorio del Roque de los Muchachos of the Instituto de Astrofisica de Canarias.

field regime of general relativity. For example, quiescent X-ray spectra and advection-dominated accretion flow (ADAF) models provide evidence for black hole event horizons (Narayan, McClintock, & Yi 1996; Garcia et al. 2001). Also, the study of high-frequency quasi-periodic oscillations (QPOs) may lead to the first secure measurement of black hole spin (e.g., Remillard et al. 1999; Strohmayer 2001).

XTE J1550−564 was discovered on 1998 September 7 by the All-Sky Monitor (ASM) onboard the *Rossi X-Ray Timing Explorer* (*RXTE*) (Smith et al. 1998). The optical counterpart (designated V381 Normae) and the radio counterpart were discovered shortly thereafter (Orosz, Jain, & Bailyn 1998; Campbell-Wilson et al. 1998). This source was quickly identified as a promising black hole candidate based on its rapid X-ray variability, hard energy spectrum, and the absence of pulsations or X-ray bursts (Cui et al. 1999; Sobczak et al. 1999b). Relativistic plasma ejections at probable superluminal velocities were observed at radio wavelengths shortly after the strong X-ray flare in 1998 September (Hannikainen et al. 2001), indicating that XTE J1550−564 is another microquasar. The Galactic microquasars are excellent laboratories for the study of relativistic jets since they evolve orders of magnitude more quickly than do the jets in quasars (Mirabel & Rodriguez 1999). XTE J1550−564 is also of special interest owing to its complex X-ray variability (e.g., Homan et al. 2001; Remillard et al. 2002). In this paper we report the results of our recent optical observations of XTE J1550−564. The observations and basic data reductions are summarized in § 2. In § 3 we establish the orbital parameters of the system, derive some properties of the secondary star, derive geometrical parameters for the binary, and discuss limits on the mass of the compact object. The implications of our results are discussed in § 4 and summarized in § 5.

2. THE OBSERVATIONS AND THEIR REDUCTIONS

2.1. *Spectroscopy*

We obtained a total of 18 spectra of the source on 2001 May 24–27 using Antu, which is the first 8.2 m telescope at the European Southern Observatory, Paranal. We used the FORS1 imaging spectrograph with the 600V grism and a 0″.7 wide slit; this combination gives a spectral resolution of 3.6 Å FWHM and a wavelength coverage of 4571–6927 Å. The seeing was better than 0″.8 on May 24 and May 27, and relatively poor on May 26 (>1″.5). Clouds were present on the night of May 25, and only one useful spectrum was obtained in 1″.5 seeing. The exposure times ranged from 20 to 40 minutes depending on the conditions. We also observed eight bright subgiant (luminosity class IV) and giant (luminosity class III) stars with spectral types from G8 to M0. An atmospheric dispersion corrector was used, and the slit was kept at the default north-south direction. Following the standard procedure at Paranal, the flat field and wavelength calibration exposures were obtained during the daytime hours with the telescope pointed at the zenith.

We reduced all of the spectra using IRAF.[2] The standard tasks were used to apply the bias and flat-field corrections, and to extract and wavelength-calibrate the spectra. The night-sky emission lines were used to make small adjustments to the wavelength scales of the spectra. The spectra were placed on an approximate flux scale using observations (taken May 27) of the white dwarf flux standards EG 274 and Feige 110. The final reduced spectra of XTE J1550−564 have typical signal-to-noise ratios in the continuum near 6 per 1.16 Å pixel at 6000 Å and about 2 per 1.16 Å pixel at 5000 Å.

We extended our grid of comparison stars by making use of archival observations. Eleven spectra of seven different stars were taken from the FORS1 archive.[3] These spectra were obtained using the 600R grism and a 0″.7 wide slit; this combination gives a spectral resolution of 3.2 Å FWHM and a wavelength coverage of 5142–7283 Å. All of the standard reductions were performed with IRAF. We also used 49 spectra of 34 different stars obtained 1995 April 30 and 1995 May 2–4 using the Cerro Tololo Interamerican Observatory (CTIO) 4 m telescope and the RC spectrograph and the Loral 3072 × 1024 CCD (see Bailyn et al. 1995; Orosz & Bailyn 1997). The spectral resolution is 3.3 Å FWHM and the wavelength coverage is 3850–7149 Å. Finally, we used moderate resolution spectra of six stars with spectral types K5 V to M0 V obtained on 2001 February 16 and 17 with the red arm of the ISIS instrument on the 4.2 m William Herschel Telescope (WHT) on La Palma. The combination of the 600R grating with the 1024 × 1024 Tek4 CCD and a 1″ slit width yields a resolution of ≈70 km s^{-1} FWHM and a wavelength coverage of 5856–6646 Å. These spectra were reduced with IRAF.

2.2. *Photometry*

We observed XTE J1550−564 2001 June 26–28 using the Magellan Instant Camera (MagIC) on the Walter Baade 6.5 m Telescope located at Las Campanas Observatory. The MagIC contains a SITe 2048 × 2048 CCD with a scale of 0″.069 pixel^{-1}. The source was observed for about 5 hr on each of the three nights in generally good conditions (0″.3–0″.7 seeing and thin cirrus) with the Sloan r', i', and z' filters. Some images in the Sloan g' filter were also obtained on the night of June 26.

XTE J1550−564 has been monitored extensively by the 1 m YALO (Yale-AURA-Lisbon-Ohio) Telescope (Bailyn et al. 1999) at CTIO since the discovery of the optical counterpart in 1998 September (Orosz, Jain, & Bailyn 1998a). The V-band data from 2001 discussed here were collected and reduced in a manner similar to previous data from this source described by Jain et al. (2001a, 2001b).

As part of the normal acquisition procedure for spectroscopy we obtained a total of nine direct V images with exposure times of 30– 90 s with VLT/FORS1 in its imaging mode. In addition, two additional direct images in B with exposure times of 120 and 200 s were taken. The image scale of FORS1 is 0″.2 pixel^{-1}, and the field of view is 6.8 × 6.8 arcmin^2.

Finally, photometry of XTE J1550−564 was obtained 2001 June 1 using the SuSI2 instrument on the Nasmyth focus of the 3.5 m New Technology Telescope (NTT) located at the European Southern Observatory, La Silla. SuSI2 is a mosaic of two 2048 × 4096, thinned, antireflection-coated EEV CCDs. We used 3 × 3 on-chip binning, yielding a scale of 0″.24 pixel^{-1} and a field of view of

[2] IRAF is distributed by the National Optical Astronomy Observatory, which are operated by the Association of Universities for Research in Astronomy, Inc., under cooperative agreement with the National Science Foundation.

[3] ESO programs 63.N-0481, 65.H-0360, and 265.D-5016.

5.5×5.5 arcmin^2. The observing conditions were quite poor: the seeing was between 1.″5 and 2.″0, and there were passing clouds. We obtained a total of 51 usable *R*-band images and four usable *V*-band images with exposure times of 3–5 minutes.

The image processing routines in IRAF were used to correct for the electronic bias and to apply the flat-field corrections to the VLT, NTT, and Magellan images. The programs DAOPHOT IIe, ALLSTAR, and DAOMASTER (Stetson 1987; Stetson, Davis, & Crabtree 1991; Stetson 1992a, 1992b) were used to compute the instrumental magnitudes of XTE J1550−564 and all of the field stars within about a 1.′2 radius. The comparison stars "A," "B," and "C" shown in Figure 2 of Jain et al. (2001b) were used to place the *B*- and *V*-band instrumental magnitudes on the standard scales. The *R*-band photometry and the Magellan photometry were left on the instrumental magnitude scales. Since some of the *V*-band images from the VLT and NTT were slightly underexposed, we averaged groups of two–four consecutive exposures together, yielding two measurements from 24 May and one measurement each from the nights of 25–27 May and 1 June.

3. ANALYSIS

3.1. *Long-Term Photometry*

Figure 1*a* shows the complete YALO *V*-band light curve together with our VLT photometry. The 2–12 keV X-ray light curve from the ASM on *RXTE* is shown in Figure 1*b*. XTE J1550−564 had an optical reflare in 2001 January (Jain, Bailyn, & Tomsick 2001c; Fig. 1*a*). Strangely enough, the corresponding outburst in X-rays was quite weak, with a peak level of less than 10 ASM counts s^{-1}. The source returned to its quiescent level by about April 20, and our *V*-band magnitudes from May 24 to 27 are fully consistent with the quiescent level: $21.83 \leq V \leq 22.24$, with typical errors of 0.04 mag.

The source was not detected in *B*, and we place a conservative lower limit of $B > 24.0 \pm 0.1$. Jain et al. (1999) had estimated $B = 22.0 \pm 0.5$ for the quiescent level based on a detection (near the plate limit) of the source on the SERC J survey print. The effective bandpass of the SERC J print is actually much redder than the standard Johnson *B* filter,[4] so the quiescent magnitude given in Jain et al. (1999) is not a proper *B* magnitude but is closer to a *V* magnitude.

3.2. *Orbital Period and Spectroscopic Elements*

We measured the radial velocities of the secondary star using the *fxcor* task within IRAF, which is an implementation of the technique of Tonry & Davis (1979). The cross-correlations were computed over the wavelength range 5000–6850 Å, excluding the Hα emission line, interstellar lines (Na D and the diffuse band near 5876 Å), and a telluric feature near 6280 Å. The spectra were continuum-subtracted prior to computing the cross-correlation, and a Fourier filter was used to remove high-frequency noise. With the exception of one spectrum from the end of the night of May 27, which had poor signal-to-noise ratio, the cross-correlation peaks were generally quite significant. The value of the Tonry & Davis "*r*"-parameter, which is a measure of the signal-to-noise in a cross-correlation, was generally in the range of 3.0–4.8. The spectrum of the K3 III star HD 181110 usually gave the best cross-correlation peaks as judged by the value of the *r*-parameter, and the spectrum of the K4 III star HD 181480 generally gave the second best cross-correlation peaks. In the analysis below we adopt the velocities measured using the K3 III template. Since the source was at or very near quiescence, we believe our radial velocities are not biased by X-ray heating.

To search for the spectroscopic period we computed a three-parameter sinusoidal fit to the 17 velocities for a dense range of trial periods between 0 and 4 days. The reduced χ^2 values for these fits are shown in Figure 2*a*. The free parameters at each trial period are the velocity semiamplitude K_2, the epoch of maximum velocity T_0(spect), and the systemic velocity γ. The best fit is at a period of $P_{\rm sp} = 1.552 \pm 0.010$ days (1 σ error), where $\chi^2_\nu = 1.38$. The two alias periods near 0.7 and 2.5 days are ruled out by their large values of χ^2_ν and by inspection of the folded velocity curves. We adopt the following spectroscopic elements with 1 σ errors: $P_{\rm sp} = 1.552 \pm 0.010$ days, $K_2 = 349 \pm 12$ km s^{-1}, and $T_0(\text{spect}) = \text{HJD } 2,452,054.296 \pm 0.014$. In order to find the true systemic velocity we must know the radial velocity of the template star. We cross-correlated the spectrum of

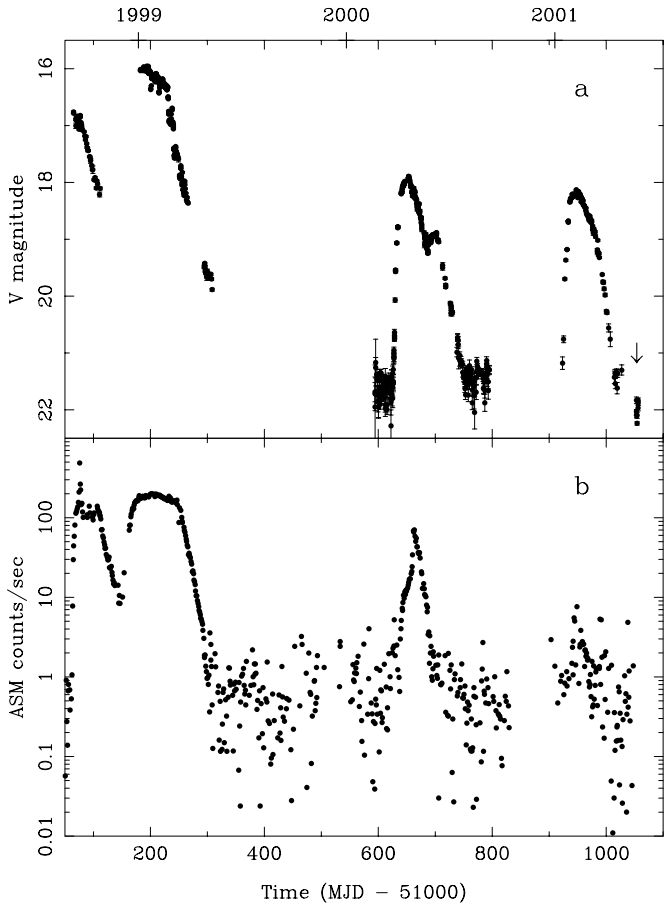

FIG. 1.—(*a*) Complete YALO *V*-band light curve of XTE J1550−564 is shown to the left of the arrow located near day 1050. The arrow indicates the time of our spectroscopic observations and our *V*-band photometric observations with VLT/FORS1, which are shown here. (*b*) The *RXTE* ASM 2–12 keV light curve of XTE J1550−564 (daily averages). The *y*-axis scale is logarithmic to highlight the weaker activity in early 2001 (the measurements with negative flux are not shown).

[4] See http://www.roe.ac.uk/ukstu/platelib.html#eqj.

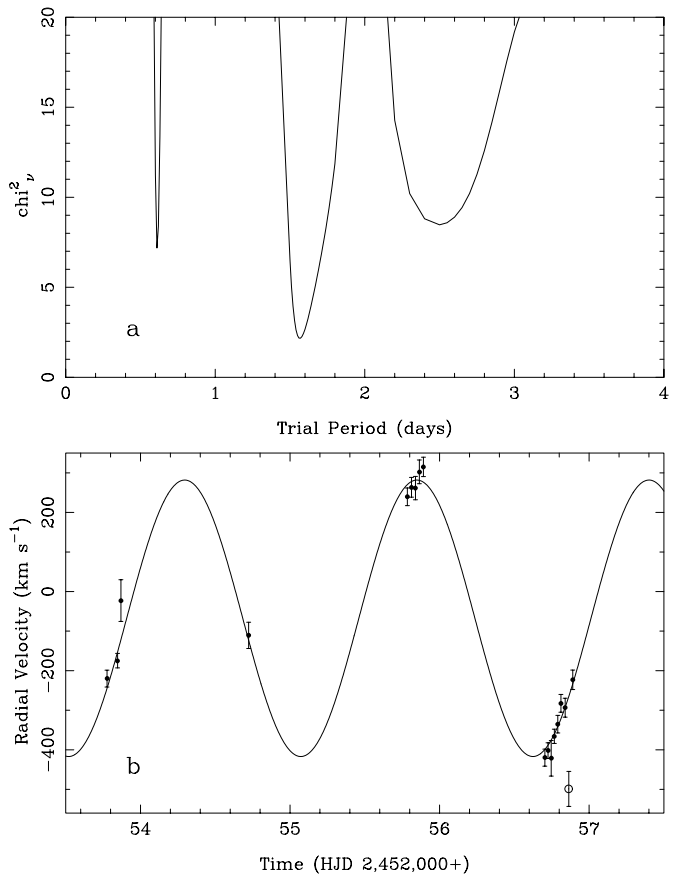

FIG. 2.—(*a*) Reduced χ^2_ν for a three-parameter sinusoidal fit to the 17 radial velocities as a function of the trial period in days. The minimum χ^2_ν is at $P = 1.552 \pm 0.010$ days, and the typical χ^2_ν value is 40. (*b*) The radial velocities and the best fitting sinusoid, plotted as a function of time. The velocity plotted as a open circle has been excluded from the fit.

HD 181110 with 47 template spectra of stars with a radial velocity measurement listed in the SIMBAD database. The median heliocentric velocity for HD 181110 was −71 km s^{-1}, and the standard deviation of the velocities was 18 km s^{-1}. Based on this, we adopt $\gamma = -68 \pm 19$ km s^{-1} for XTE J1550−564. The velocities and the best fitting sinusoid are shown in Figure 2*b*, and the spectroscopic elements are listed in Table 1. (The velocity plotted as an open circle in Figure 2*b* was excluded from the fit since it deviates by more than 4 σ from the fit.) We note that our spectroscopic period is consistent with the photometric period of $P_{\rm ph} = 1.541 \pm 0.009$ days found by Jain et al. (2001b). The optical mass function is then

$$f(M) \equiv \frac{P_{\rm sp} K_2^3}{2\pi G} = \frac{M_1^3 \sin^3 i}{(M_1 + M_2)^2} = 6.86 \pm 0.71\ M_\odot \quad (1)$$

(1 σ error). The optical mass function places an immediate lower limit on the mass of the compact object, and since this minimum mass of the compact object is well above the maximum mass of a stable neutron star ($\approx 3\ M_\odot$; Chitre & Hartle 1976; Kalogera & Baym 1996), we conclude that XTE J1550−564 contains a black hole. See § 3.5 for further discussion of the mass of the black hole.

TABLE 1

ORBITAL PARAMETERS FOR XTE J1550−564

Parameter	Value
$P_{\rm sp}$, spectroscopic orbital period (days)	1.552 ± 0.010
$P_{\rm ph}$, photometric orbital period (days)	1.5437 ± 0.0005
K_2 velocity (km s^{-1}).....	349 ± 12
γ velocity (km s^{-1}).....	-68 ± 19
T_0, spectroscopic[a] (HJD 2,452,000+)	54.296 ± 0.014
T_0, photometric[b] (HJD 2,452,000+).....	55.448 ± 0.010
Mass function ($M_\odot$)	6.86 ± 0.71

NOTE—All quoted uncertainties are 1 σ.

[a] The time of the maximum radial velocity of the secondary star.

[b] The time of the inferior conjunction of the secondary star.

3.3. *Parameters for the Secondary Star*

Using the spectroscopic ephemeris in Table 1, the 11 spectra with the highest signal-to-noise ratio were Doppler-corrected to zero velocity and averaged to create a "rest-frame" spectrum. The rest-frame spectrum was dereddened using the extinction law of Cardelli, Clayton, & Mathis (1989), where we adopted a visual extinction of $A_V = 4.75$ mag [$N_{\rm H} = (8.5^{+2.2}_{-2.4}) \times 10^{21}$ cm^{-2} (Tomsick, Corble, & Kaaret 2001) and $A_V = N_{\rm H}/1.79 \times 10^{21}$ (Predehl & Schmitt 1995)]. The true extinction is unlikely to be greater than 4.75 mag, since the extinction derived from X-ray measurements of $N_{\rm H}$ nearly always exceeds the optically measured value (Vtrilek et al. 1991).

3.3.1. *Spectral Type and Effective Temperature*

We used the technique outlined in Marsh, Robinson, & Wood (1994) to decompose the rest-frame spectrum into its disk and stellar components. For this purpose we have three sets of template spectra: eight spectra of eight different stars taken with the FORS1 600V grism (resolution ∼3.6 Å), 11 spectra of seven different stars taken with the FORS1 600R grism (resolution ∼3.6 Å), and 49 spectra of 34 different stars taken at CTIO (resolution ∼3.3 Å). The dereddened rest-frame spectrum and the template spectra were all normalized to unity at 6000 Å and resampled to a pixel size of 1.155 Å. The template spectra were then scaled by various values of a weight factor w between 0.0 and 1.0 in steps of 0.02 and subtracted from the rest-frame spectrum. The scatter in each difference spectrum was measured by fitting a low-order polynomial and computing the rms difference over the same wavelength region used for the cross-correlation analysis above. For each template spectrum we looked for the value of w that gave the "smoothest" difference spectrum (i.e., the w with the lowest associated rms). Figure 3 shows the rms values as a function of the template spectral type for the three sets of templates. Since the spectral resolution in each of the three sets is slightly different, one should only compare the rms values within a single set. For the CTIO grid the minimum rms is near spectral type G6. However, the difference spectra for the G6 templates (and the templates of earlier type) have negative flux in the blue parts of the spectrum, which is unphysical. This difficulty could be lessened if one were to adopt a larger value of A_V; however, values larger than $A_V = 4.75$ mag are unlikely (see above). The templates with spectral type G8 and later, on the other hand, all produce subtracted spectra with positive differences. The minimum rms values for the FORS1

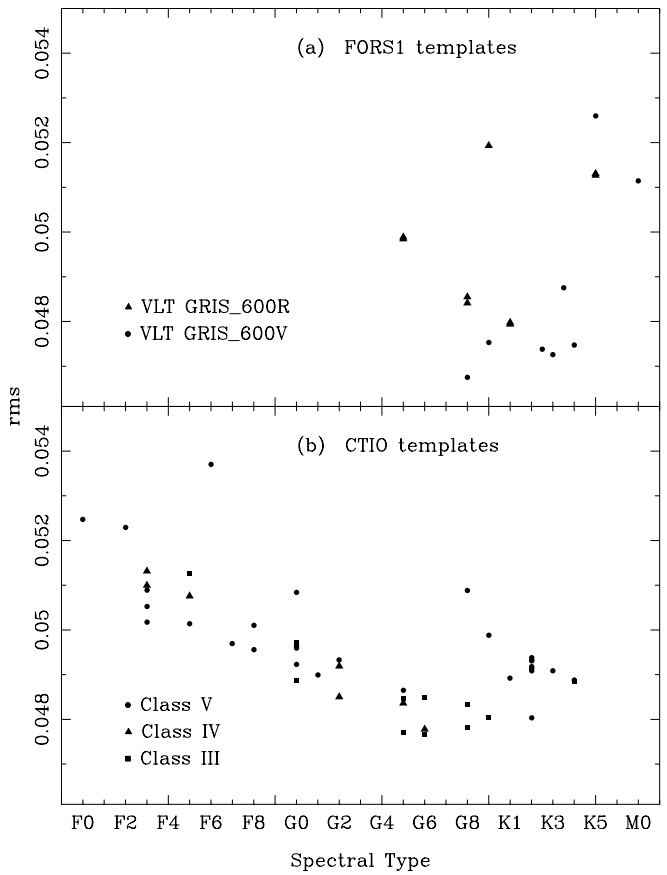

FIG. 3.—(*a*) Rms values of the polynomial fits to the difference spectra as a function of the template spectral type for the templates obtained with VLT/FORS1 (luminosity class III and IV). The plotting symbols indicate the grism used. (*b*) Same as (*a*) but for the templates observed at CTIO. Here the plotting symbols indicate the luminosity class of the template.

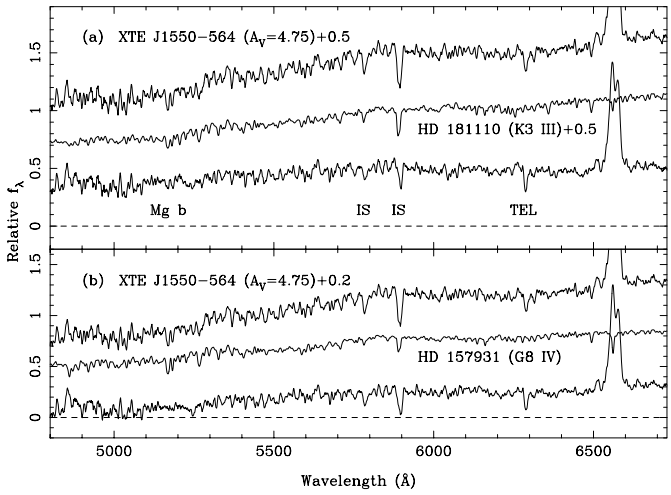

FIG. 4.—Results of the spectral decomposition. (*a*) *Top line:* The dereddened rest-frame spectrum of XTE J1550−564, smoothed to 5 pixels and offset by 0.5 units. *Middle line:* The spectrum of the K3 III star HD 181110, scaled by 0.48 and offset by 0.5 units. *Bottom line:* The difference spectrum, which represents the spectrum of the accretion disk, smoothed to 5 pixels with no offset. The interstellar features are denoted by IS, and the telluric feature is denoted by TEL. (*b*) *Top line:* The dereddened rest-frame spectrum of XTE J1550−564, smoothed to 5 pixels and offset by 0.2 units. *Middle line:* The spectrum of the G8 IV star HD 157931, scaled by 0.74 with no offset. *Bottom line:* The difference spectrum smoothed to 5 pixels with no offset.

templates is at spectral type G8 for the grism 600V and spectral type K1 for the grism 600R. In general, there is a steep rise in the rms values for template spectral types later than K5 and earlier than G5. The weight factor w is roughly correlated with the template spectral type where templates with later spectral types have smaller values of w.

Figure 4 shows the rest-frame spectrum decomposed into the disk and stellar components for two different templates observed with the FORS1 grism 600V (i.e., the same instrumental configuration used for the XTE J1550−564 spectra). Figure 4*a* shows the decomposition using the K3 III template HD 181110 ($w = 0.48$) and Figure 4*b* shows the decomposition using the G8 IV template HD 157931 ($w = 0.74$). In both cases the disk spectrum is basically flat in F_λ, and the only obvious features remaining are the Hα emission line, the interstellar lines, and the telluric line (note that these features have been smeared in the process of making the rest-frame spectrum). The Mg b lines near 5169 Å are matched better with the G8 IV template. Apart from Mg b, the two difference spectra look very similar to the eye.

Based on the decomposition analysis above, we adopt a spectral type of G8–K4 for the secondary star. The spectral type is almost certainly not K7 or later since the TiO bands near 6230 and 6700 Å become apparent in dwarfs at K7 and later and in giants at K5 and later, and these bands are not evident in our spectrum. Spectral types earlier than about G5 are also firmly ruled out based on the high rms values (Fig. 4*b*) and the partly negative difference spectra. The secondary star cannot have a normal main-sequence gravity owing to the relatively long orbital period, so its surface gravity must be somewhat less than the nominal values for luminosity class V. The surface gravity of the secondary is easily found using Kepler's third law, assuming that the star fills its Roche lobe. In that case, there is a relationship between the mean density of the secondary star and the orbital period:

$$\rho = \frac{M_2}{4/3\ \pi R_2^3} = \frac{3\pi}{P^2 G R_{\rm RL}^3(Q)} \frac{1}{1+Q}\ , \qquad (2)$$

where $R_{\rm RL}(Q)$ is the sphere-equivalent radius of the Roche lobe for unit separation and G is the universal constant of gravity. One can readily show through numerical integration that for $2 \le Q \le 20$, the quantity $R_{\rm RL}^{-3}(Q)(1+Q)^{-1}$ only varies by 4.6% (between 9.7 and 10.2). Hence, for a fixed orbital period P, the mean density of the secondary is nearly independent of the mass ratio Q. This in turn means that the resulting surface gravity is a very weak function of the assumed secondary star mass M_2 ($\log g \propto \frac{1}{3}\log M_2$). We find surface gravities of $\log g = 3.51$, 3.61, and 3.72 for secondary star masses of 0.5, 1.0, and 2.0 $M_\odot$, respectively. These values of $\log g$ imply a luminosity class between III and V (e.g., a K4 V star nominally has $\log g = 4.60$ and a K4 III star nominally has $\log g = 1.7$; Gray 1992). The temperature corresponding to a given spectral type depends on the luminosity class, where main-sequence stars of a given spectral type (i.e., luminosity class V) are hotter than the corresponding giants (luminosity class III). Straižys & Kuriliene (1981) give $T_{\rm eff} \sim 4100$ K for a K4 III star and $T_{\rm eff} \sim 5100$ K for a G8 IV star. Thus we adopt $4100 \le T_{\rm eff} \le 5100$ K for the analysis below.

3.3.2. *Rotational Broadening*

We used the Marsh et al. (1994) technique to estimate the projected rotational velocity $V_{\rm rot} \sin i$ of the XTE J1550−564 rest-frame spectrum. The dereddened rest-frame spectrum, the spectrum of the G8 IV star HD 157931, and the spectrum of the K3 III star HD 181110 were each normalized to unity at 6000 Å and resampled to a pixel size of 0.46 Å. An IRAF procedure implementing the analytic broadening kernel given in Gray (1992, p. 374) was used to broaden the template spectrum using values of $V_{\rm rot} \sin i$ between 50 and 160 km s^{-1} in steps of 5 km s^{-1} (we adopted a linear limb darkening coefficient of 0.6). The value of the weight factor w was optimized to find the minimum rms value at each input value of $V_{\rm rot} \sin i$. The results are shown in Figure 5*a*. The minimum rms value occurs for $V_{\rm rot} \sin i = 90$ km s^{-1} for the G8 IV template and at $V_{\rm rot} \sin i = 95$ km s^{-1} for the K3 III template.

We next attempted to measure $V_{\rm rot} \sin i$ for the secondary star using a different technique that is based on the relationship between the width of the cross-correlation (cc) peak and the rotational velocities of the object and template spectra (Horne, Wade, & Szkody 1986; Echevarría et al. 1989; Casares et al. 1993). A Gaussian with a fitting width of 750 km s^{-1} and a baseline of zero was used to determine the width of the cc peaks. The measured widths were relatively insensitive to the exact width of the fitting region. The FWHM of the rest-frame spectrum cc peak is in the range of 285–305 km s^{-1}, depending on which template is used. In order to find out what rotational velocity this corresponds to, we constructed calibration curves using some bright comparison stars observed with the FORS1 600V grism. Three different comparison stars were each broadened by various amounts, and the FWHM of the cc peaks were measured using the K3 III template HD 181110. The results are shown in Figure 5*b*. These calibration curves show that a cc peak FWHM of 305 km s^{-1} corresponds to a rotational velocity of $V_{\rm rot} \sin i \approx 90$ km s^{-1} and that a FWHM of 285 km s^{-1} corresponds to an input $V_{\rm rot} \sin i$ of about 50 km s^{-1}.

The Marsh et al. (1994) technique indicates a rotational velocity of $V_{\rm rot} \sin i = 90$ km s^{-1} (given the better performance of the G8 template in separating the star and disk spectra we adopted the value of $V_{\rm rot} \sin i$ measured with this template; Fig. 5*a*), and the cross-correlation technique indicates $V_{\rm rot} \sin i \lesssim 90$ km s^{-1} (Fig. 5*b*). Based on the results of the two techniques, we adopt a value of $V_{\rm rot} \sin i = 90 \pm 10$ km s^{-1} for the rotational velocity of the secondary star.

The value of $V_{\rm rot} \sin i$ should be treated with caution since our spectral resolution is relatively low (about 160 km s^{-1}) and the signal-to-noise ratio is modest (about 20 per pixel in the rest-frame spectrum). In order to have some idea of the size of the systematic errors involved with measuring the rotational velocity in a relatively noisy low-resolution spectrum, we performed some numerical experiments using the moderate resolution spectra obtained with the WHT. These experiments are by no means comprehensive since we have only a limited range of spectral types (K5 to M0, all dwarfs) and wavelength coverage (roughly between the Na D lines and Hα). The six template spectra were first normalized at a common wavelength (6450 Å). A simulated object spectrum was made as follows: a template was scaled by 0.7, rotationally broadened by 90 km s^{-1}, degraded to a resolution of 3.6 Å by convolution with a Gaussian, and resampled to 1.16 Å (to match the pixel size of the VLT/FORS1 spectra). Next, a constant value of 0.3 was added (to simulate the accretion disk), and Gaussian noise was added so that the signal-to-noise ratio was ≈20. Finally, the simulated object spectrum and the remaining template spectra were resampled to a pixel size of 0.46 Å. The rotational velocity of the simulated object spectrum was extracted by the two different techniques, and the results are shown in Figures 5*c* and 5*d*. The Marsh et al. technique gives a rotational velocity of just over 100 km s^{-1} using the two best-matched templates, and the cross-correlation technique gives a rotational velocity between about 80 and 110 km s^{-1} using all templates and between about 100 and 110 km s^{-1} using the two best-

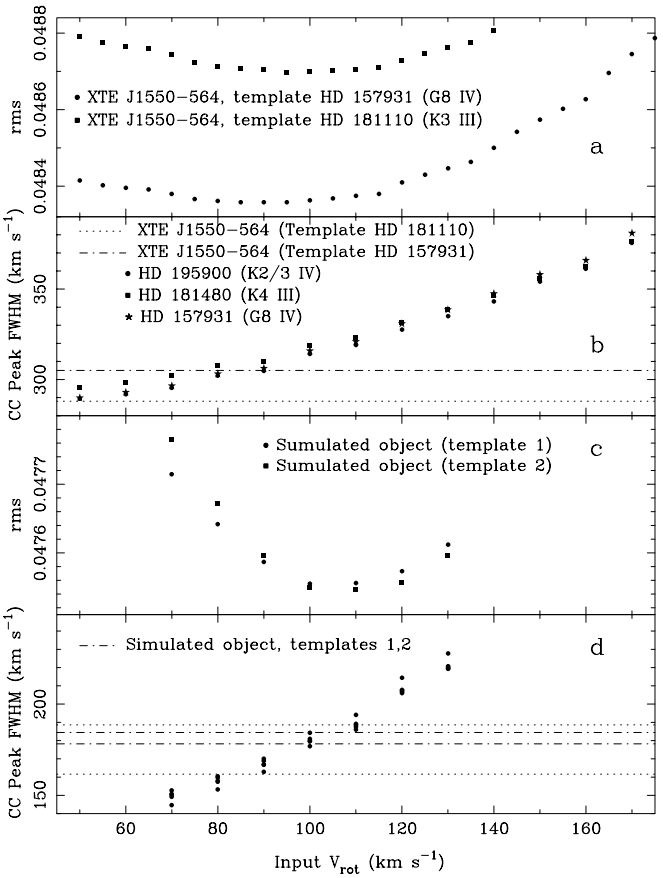

FIG. 5.—(*a*) Rms values of the polynomial fits to the difference spectra as a function of the input value of the rotational velocity $V_{\rm rot} \sin i$. The lowest rms value is for $V_{\rm rot} \sin i = 90$ km s^{-1} for the G8 IV template HD 157931 (*filled circles*) and $V_{\rm rot} \sin i = 95$ km s^{-1} for the K3 III template HD 181110 (*filled squares*). (*b*) The FWHM of the cross-correlation peaks of three different comparison star spectra as a function of the input value of the rotational velocity $V_{\rm rot} \sin i$. In all cases the template spectrum for the cross-correlation analysis was the K3 III star HD 181110. The lines show the width of the cross-correlation peak for the XTE J1550−564 rest-frame spectrum measured using two different template spectra (the dotted line for the K3 III template HD 181110 and the dash-dotted line for the G8 IV template HD 157931). The results in (*a*) and (*b*) show that the rotational broadening of XTE J1550−564 is on the order of 90 km s^{-1} or less. (*c*) Similar to (*a*), but for a simulated spectrum constructed with a moderate resolution spectrum (≈70 km s^{-1} FWHM), using an input value of $V_{\rm rot} \sin i = 90$ km s^{-1}. (*d*) Similar to (*b*), but for the simulated spectrum and the moderate-resolution templates. The dotted lines show the full range of the width of the cross-correlation peak for the simulated object spectrum measured with all six templates, and the dash-dotted lines show the width of the cross-correlation peak measured with the two best matched templates. The results in (*c*) and (*d*) show that the systematic error involved in measuring the rotational velocity in a relatively noisy low-resolution spectrum is not too large and is perhaps on the order of about 10 km s^{-1}.

matched templates. Given that the input rotational velocity for the simulated spectrum was 90 km s^{-1}, we conclude that the systematic errors involved in this technique are not excessively large and are probably on the order of our adopted 1 σ error of 10 km s^{-1}. Needless to say, it would be desirable to repeat the measurement of the rotational velocity of the secondary star in XTE J1550−564 using data with better resolution and a higher signal-to-noise ratio.

If the secondary star is rotating synchronously with the orbit, its mean rotational velocity depends only on the binary mass ratio $Q \equiv M_1/M_2$ and the projected orbital velocity K_2 (e.g., Horne, Wade, & Szkody 1986). We used the ELC code (Orosz & Hauschildt 2000) to numerically compute sphere-equivalent Roche lobe radii as a function of the mass ratio Q and a simple Monte Carlo code to propagate the (1 σ) uncertainties on the input parameters. We find $Q = 6.6^{+2.5}_{-1.6}$ (1 σ) for $K_2 = 349 \pm 12$ km s^{-1} and $V_{\rm rot} \sin i = 90 \pm 10$ km s^{-1}. This mass ratio is relatively far from unity, which is typical of X-ray novae with cool low-mass companions (e.g., Bailyn et al. 1998 and references therein).

3.4. *The* Hα *Profile*

The XTE J1550−564 spectra show a strong, double-peaked Hα emission line. Figure 6 shows the mean Hα line profile obtained by averaging the 11 spectra with the highest signal-to-noise. The equivalent width of the line is about 24.7 Å, the FWHM is about 1500 km s^{-1}, and the maximum velocity in the line wings is about 1000 km s^{-1}. We do not detect any feature at the wavelength of Hβ, although the signal-to-noise is rather poor there.

The double-peaked emission line is characteristic of emission from an accretion disk (Smak 1981). In this case there is $\lesssim$8% stellar contribution to the Hα profile since late-G and early-K stars have relatively weak Hα absorption lines (EW $<$ 2 Å, Fig. 4). We modeled the line profile using a simple model outlined in Smak (1981; see also Johnston, Kulkarni, & Oke 1989, and Orosz et al. 1994). The three main parameters are (1) the power-law exponent α, which determines the density function of the emitting atoms, $f(r) \propto r^{-\alpha}$ (where the coordinate r is normalized to 1 at the outer edge of the disk); (2) the ratio r_1 of the inner disk radius to the outer disk radius; and (3) the radial velocity v_d of the outer edge of the disk. Horne & Marsh (1986) have modified the model to include profiles from an optically thick disk; this modification requires that the inclination be included as an additional parameter. An optically thin model with $\alpha = 2$, $r_1 = 0.17$, and $v_d = 420$ km s^{-1} provides a reasonably good match to the observed profile (we have made no attempt to optimize the model fits), although there is some excess emission in the blue line wing and the central depression in the observed profile is deeper than the model (see Fig. 6). The optically thick models have deeper central depressions, and the depth of an optically thick model with $i = 50°$ (and $\alpha = 2$, $r_1 = 0.17$, and $v_d = 420$ km s^{-1}; Fig. 6) matches the depth of the central depression reasonably well. One should note that the inclination used in the model profile may not be a good indicator of the actual binary inclination (see § 3.5). For example, the depth of the central depression in the Hα profile of GS 1124−683 (XN Mus 91) was observed to vary over an orbital cycle (Orosz et al. 1994).

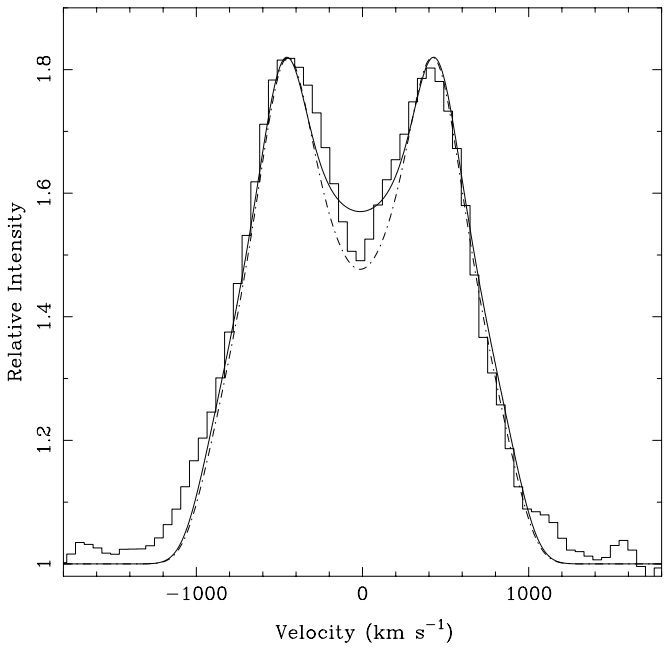

FIG. 6.—Mean Hα profile is plotted as the "histogram." The y-axis scale is arbitrary, with the continuum level at $y = 1$. Two model profiles are shown are an optically thin model with $\alpha = 2$, $r_1 = 0.17$, and $v_d = 420$ km s^{-1} (*solid line*) and an optically thick model with $\alpha = 2$, $r_1 = 0.17$, $v_d = 420$ km s^{-1}, and $i = 50°$ (*dash-dotted line*).

The line wings of the Hα profile of XTE J1550−564 are relatively steep and do not extend to very high velocities (slightly more than 1000 km s^{-1}). In contrast, the line wings of the Hα profile of GS 1124−683 and H1705−250 (XN Oph 77) extend out to almost 2000 km s^{-1} (Orosz et al. 1994; Remillard et al. 1996). For A0620−00, the width of the Hα profile has been observed to vary between these extremes during 1991–1993 (Orosz et al. 1994). The weakness or absence of the Hβ line in XTE J1550−564 is similar to what is observed in H1705−250 in 1994 (Remillard et al. 1996). There is some excess emission in the blue line wing of the XTE J1550−564 Hα profile. Excess emission in the blue-line wing was observed in GS 1124−683 in 1992, but not in 1993, and in A0620−00 in 1991, but not in 1993. Finally, we note that the ratio of the disk velocity v_d to the K-velocity in XTE J1550−564 is $v_d/K_2 = 1.2$. This value is well within the range observed for the other black hole X-ray novae with (cool) low-mass companions (see Table 2). Thus in terms of the properties of its quiescent accretion disk, XTE J1550−564 appears to be a typical black hole system.

3.5. *Ellipsoidal Light-Curve Models and Derived Astrophysical Parameters*

The value of the orbital inclination i is needed to compute the component masses and other interesting parameters. Normally one models the ellipsoidal light curves to estimate the inclination of a semidetached system such as XTE J1550−564, and for this purpose we used the ELC code (Orosz & Hauschildt 2000). The model has many free parameters. The binary parameters for a circular orbit are the inclination i, the mass ratio Q, the orbital separation a, the orbital period P, and the epoch of the inferior conjunction of the secondary star T_0(photo). The main parameters for the secondary star are its mean temperature $T_{\rm eff}$, its gravity-darkening exponent β, its Roche lobe filling factor f, and its rotational velocity with respect to synchronous Ω.

TABLE 2
DISK VELOCITIES FOR BLACK HOLE SYSTEMS

Object Name	v_d/K_2	Reference
H1705−250.....	1.11	1
GS 1124−683.....	1.13	2
GRO J0422+32.....	1.17	3, 4
XTE J1550−564.....	1.20	5
A0620−00[a]	1.24	2
GRS 1009−45.....	1.26	6
V404 Cyg	1.33	7, 8
GS 2000+25.....	1.35	9
A0620−00[b]	1.47	2

REFERENCES.— (1) Harlaftis et al. 1997; (2) Orosz et al. 1994; (3) Orosz & Bailyn 1995; (4) Filippenko, Matheson, & Ho 1995; (5) this work; (6) Filippenko et al. 1999; (7) Casares, Charles, & Naylor 1992; (8) Gotthelf et al. 1992; (9) Filippenko, Matheson, & Barth 1995.
[a] Observed 1991 profile.
[b] Observed 1993 profile.

Finally, there are parameters related to the accretion disk, which are the outer radius of the disk $r_{\rm out}$, the inner radius of the disk $r_{\rm in}$, the opening angle of the outer disk rim $\beta_{\rm rim}$, the temperature at the inner edge $T_{\rm disk}$, and the power-law exponent on the disk temperature profile ξ, where $T(r) = T_{\rm disk}(r/r_{\rm in})^{\xi}$. Some of these parameters can be fixed at reasonable values. We assume the secondary star exactly fills its Roche lobe and is in synchronous rotation. Hence $f = \Omega = 1$. Following Claret (2000) the value of the gravity-darkening exponent β is a function of the mean temperature of the secondary star. In this case the gravity-darkening exponent is in the range of $0.06 \leq \beta \leq 0.11$ for our adopted temperature range of $4100 \leq T_{\rm eff} \leq 5100$ K. We used the specific intensities from the NextGen models (Hauschildt, Allard, & Baron 1999a, 1999b), so consequently no parameterized limb-darkening law was needed. The inner radius of the disk was taken to be 3% of the compact object's Roche lobe radius, which is roughly 10^4 Schwarzschild radii (see Hameury et al. 1997).

We are left with 10 free parameters in the ellipsoidal model: Q, i, a, P, T_0(photo), $T_{\rm eff}$, ξ, $T_{\rm disk}$, $r_{\rm out}$, and $\beta_{\rm rim}$. For a given ellipsoidal model, we can compute various observable quantities such as the shape of the light curves in a given bandpass, the amplitude and phasing of the radial velocity curve of the secondary star, the amount of disk light in various bandpasses, and the radius, gravity, and rotational velocity of the secondary star, etc. The goal is to find the set of model parameters that gives the best fit to all the observed properties of XTE J1550−564.

To accomplish the optimization goal we used a genetic optimization code based on the *pikaia* routine given in Charbonneau (1995), with the "Black Sheep" modification outlined by Bobinger (2000). This genetic code is very efficient at finding the global optimal solution in a large parameter space (see Charbonneau 1995 and Metcalfe 2001[5] for more detailed discussions of genetic algorithms). The algorithm used in the code is quite simple. We define a "population" of 100 random parameter sets. For each parameter set we compute the ellipsoidal model and define a "fitness" based on how well the particular model compares with the available observations. After the fitness of the initial population is determined, 100 new parameter sets are produced as a result of "breeding" between pairs of members, where the probability of breeding is based on the fitness. Random variations (i.e., "mutations") are introduced into a small fraction of the breeding events. The process of breeding a new population and evaluating its members is repeated (i.e., the population "evolves") over many generations (typically a few hundred or more) until convergence is achieved.

We will use the χ^2 statistic to evaluate the goodness-of-fit between the predicted and observed light and velocity curves:

$$\chi^2_{\rm total} = \chi^2_{\rm light} + \chi^2_{\rm velocity} = \sum_{j=1}^{6}\sum_{i=1}^{N_j}\frac{[y(x_i; a_1 \ldots a_{10}) - y_i]^2}{\sigma_i^2} + \sum_{i=1}^{17}\frac{[y(x_i; a_1 \ldots a_{10}) - y_i]^2}{\sigma_i^2}. \quad (3)$$

Here the notation $y(x_i; a_1 \ldots a_{10})$ means the "model value computed at x_i" and y_i means the "observed quantity at the same x_i." There is a double summation in the $\chi^2_{\rm light}$ term because we have six filters. In the genetic code, the fitness of a population member is related to its relative value of the χ^2. The member with the lowest χ^2 has the highest fitness, the one with the second lowest χ^2 has the second highest fitness, and so on. We can also consider at least three additional measures of fitness: (1) For each model we can predict Θ, the duration of an X-ray eclipse, if any. In the case of XTE J1550−564, the X-ray eclipse duration is $\Theta = 0$ at a high level of confidence since there were no eclipses observed in the almost 300 pointed *RXTE* observations of XTE J1550−564 during its various outbursts nor in the extensive *RXTE* ASM observations (Fig. 1*b*). Thus we have

$$\chi^2_{\Theta} = \begin{cases} 0 & \text{if } \Theta = 0\,, \\ 10^6 & \text{if } \Theta > 0\,. \end{cases} \quad (4)$$

As a result of this definition of χ^2_{Θ}, any model where the X-ray source is eclipsed is assigned a very low fitness. (2) For each model we can predict k_V, which is the fraction of the V-band light contributed by the accretion disk. Observationally, k_V can be estimated using the decompositions discussed in § 3.3. At 5500 Å, the disk fraction is ≈0.4 for the K3 III template (Fig. 4*a*), and ≈0.2 for the G8 IV template (Fig. 4*b*). For the purposes of the ellipsoidal modeling we will adopt $k_V = 0.3 \pm 0.1$. We then have

$$\chi^2_{k_V} = \frac{[k_V(a_1 \ldots a_{10}) - 0.3]^2}{0.1^2}\,. \quad (5)$$

For simplicity we will neglect the small correlation between the disk fraction and the effective temperature. (3) For each model we can predict $V_{\rm rot}\sin i$, which is the value of the projected rotational velocity of the secondary star. In § 3.3.2 we tentatively measured $V_{\rm rot}\sin i = 90 \pm 10$ km s^{-1}. We then have

$$\chi^2_{\rm rot} = \frac{[V_{\rm rot}\sin i(a_1 \ldots a_{10}) - 90]^2}{10^2}\,. \quad (6)$$

Our total χ^2 becomes $\chi^2_{\rm total} = \chi^2_{\rm light} + \chi^2_{\rm vel} + \chi^2_{\Theta} + \chi^2_{k_V} + \chi^2_{\rm rot}$.

[5] See http://whitedwarf.org/metcalfe.

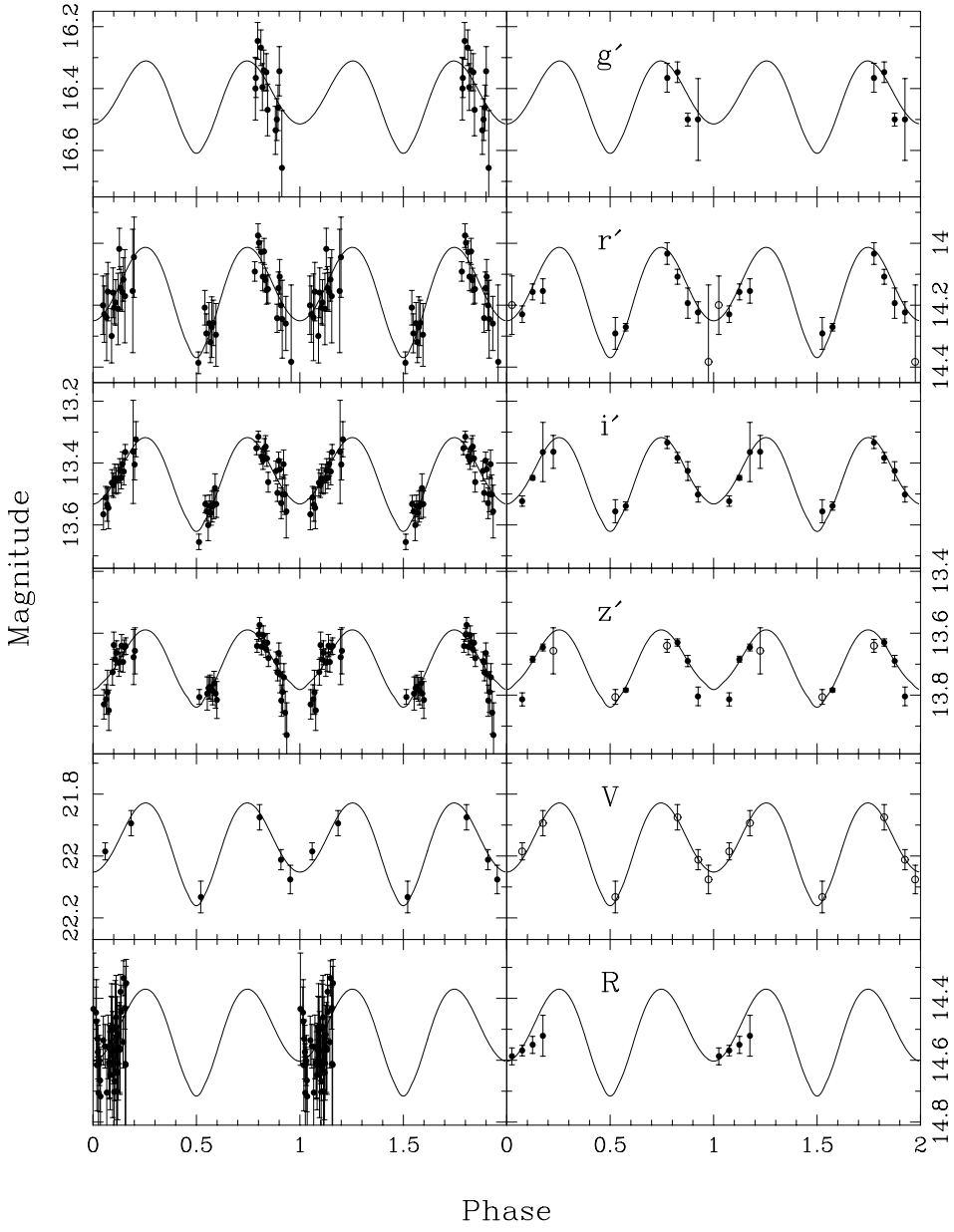

FIG. 7.—Left panels show the folded light curves in the Sloan g', r', i', and z' filters and the Bessell V and R filters and the best-fitting ellipsoidal models. Note that only the V-band data are calibrated onto the standard scale. The smoothed light curves shown in the right panels were made by computing the median magnitude within bins 0.05 phase units wide. Bins with a single point are denoted by open circles.

In any optimization procedure, one must decide how to assign weights to the observations. In our case some initial fits were performed to get an approximate solution. Based on these initial results, the error bars on the photometric measurements were scaled slightly to give $\chi^2_{\rm light}/\nu \approx 1$ at the minimum in *each* of the six filters separately. Similarly, the errors on the radial velocities were scaled to give $\chi^2_{\rm vel}/\nu \approx 1$ at the minimum.

Since our measured value of the rotational velocity may have a large systemic error (the value we measured is smaller than the spectral resolution), we ran two sets of fits. Fitting run A did *not* include the contribution of $V_{\rm rot} \sin i$ in the total χ^2. Fitting run B *did* include the observed value of $V_{\rm rot} \sin i = 90$ km s^{-1} in the total χ^2 (i.e., we are taking the value of 90 km s^{-1} at face value). For each of the two fitting runs A and B, the genetic fitting code was run six separate times on the data with the scaled error bars, using a population size of 100. The volume of parameter space that was searched was the same in all six cases, but the order in which the parameters were encoded into the "genes" was different. In practice this means that the initial random populations were different, and the way two population members exchange parameters when breeding was different. In all cases the final best-fitting parameters were statistically identical after about 200 generations, giving us great confidence that our solutions for each of runs A and B are truly the global ones.

The folded light curves in the six bands and the model light curves are shown in Figure 7. Although we fit the unbinned data, we also show in Figure 7 smoothed versions of the light curves that were made by computing the magnitude within bins 0.05 phase units wide. The

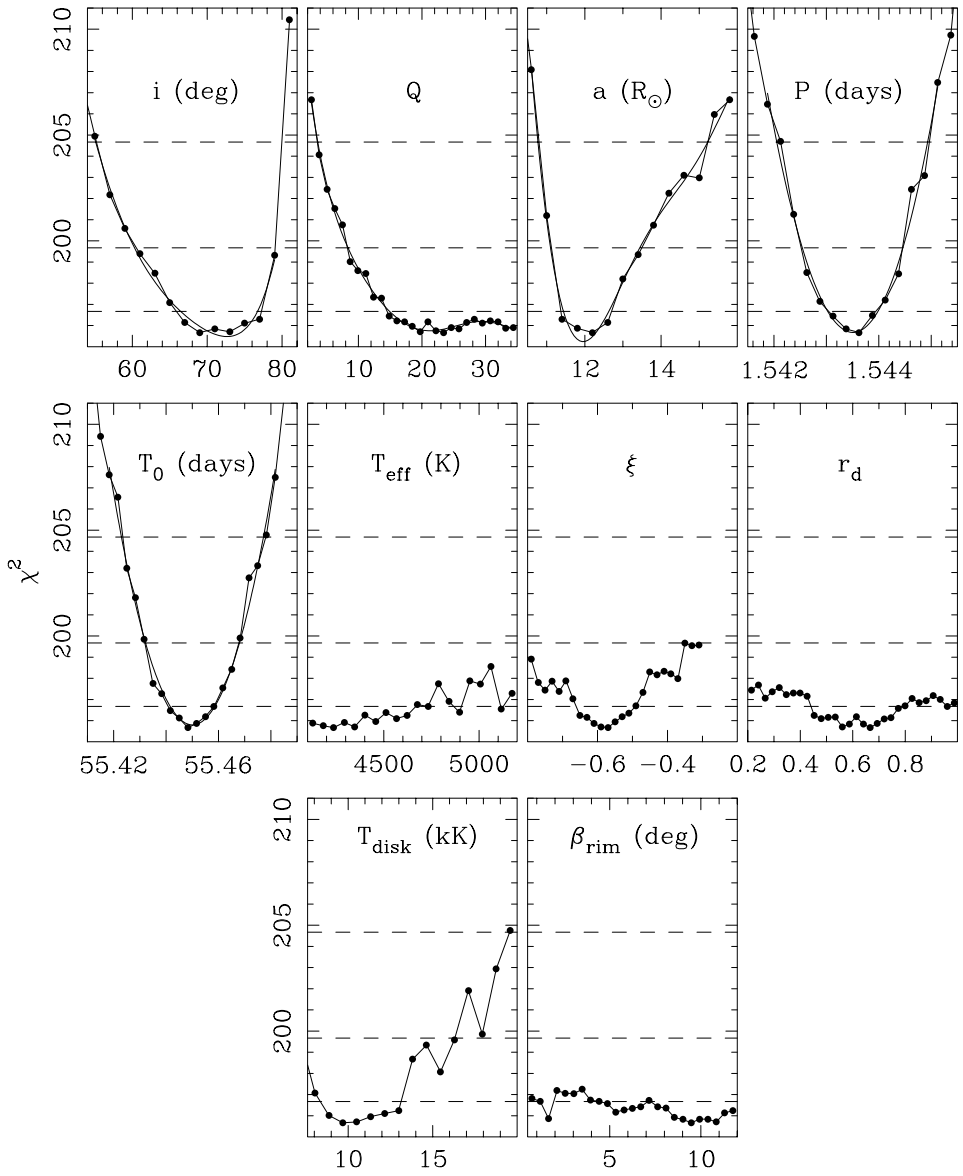

FIG. 8.—The χ^2 values as a function of the 10 fitting parameters for the fitting run A (the run without a $V_{\rm rot} \sin i$ constraint). They are, from left to right and top to bottom, the inclination i in degrees, the mass ratio Q, the orbital separation a in solar radii, the orbital period P in days, the phase zero-point T_0 in days since HJD 2,452,000, the mean temperature of the secondary star $T_{\rm eff}$, the power-law exponent ξ on the disk temperature profile, the radius of the outer edge of the disk r_d as a fraction of the compact object's Roche lobe radius, the temperature of the inner edge of the disk $T_{\rm disk}$ in units of 1000 K, and the opening angle of the outer rim of the disk $\beta_{\rm rim}$ in degrees. Fifth- or sixth-order polynomial fits to the first five curves used to get the confidence regions are shown as the smooth lines. The dashed lines denote the 1, 2, and 3 σ confidence limits.

smoothed light curves generally follow the fitted models quite well.

In order to estimate the uncertainties on the fitted parameters and the uncertainties on the derived astrophysical parameters we collapse the 10-dimensional χ^2 function onto the appropriate parameter of interest. The 1, 2, and 3 σ confidence limits are then the values of the parameter where $\chi^2 = \chi^2_{\rm min} + 1, \chi^2_{\rm min} + 4$, and $\chi^2_{\rm min} + 9$, respectively. Using the genetic fitting code and the Black Sheep modification it is quite easy to compute these confidence limits since the region of parameter space near the χ^2 minimum is sampled quite well. For each model that is computed, the χ^2 of the fit, the values of the free parameters, and the computed astrophysical parameters (e.g., the black hole mass, the secondary star radius, etc.) are saved. After a sufficiently large number of models have been computed (more than 515,000 in fitting run A and 465,000 in fitting run B), we can collapse the χ^2 function onto the parameter of interest by simply plotting the χ^2 versus the parameter of interest and looking at the "lower envelope" (i.e., the minimum χ^2 within small bins over the whole range).

Figure 8 shows the collapsed χ^2 function for the 10 fitted parameters in the fitting run A, and Figure 9 shows the similar plot for the fitting run B. In some cases, we fitted fifth- or sixth-order polynomials to the curves to more objectively to determine the value of the parameter where $\chi^2 = \chi^2_{\rm min}$ and the 1, 2, and 3 σ confidence limits. In general, the important geometrical parameters in the ellipsoidal model (i.e., the inclination i, separation a, etc.) have well-defined minima and 3 σ limits. In addition, the derived parameter ranges are not too different between fitting run A and fitting run B. The one exception is the mass ratio Q. In the fitting run A, where

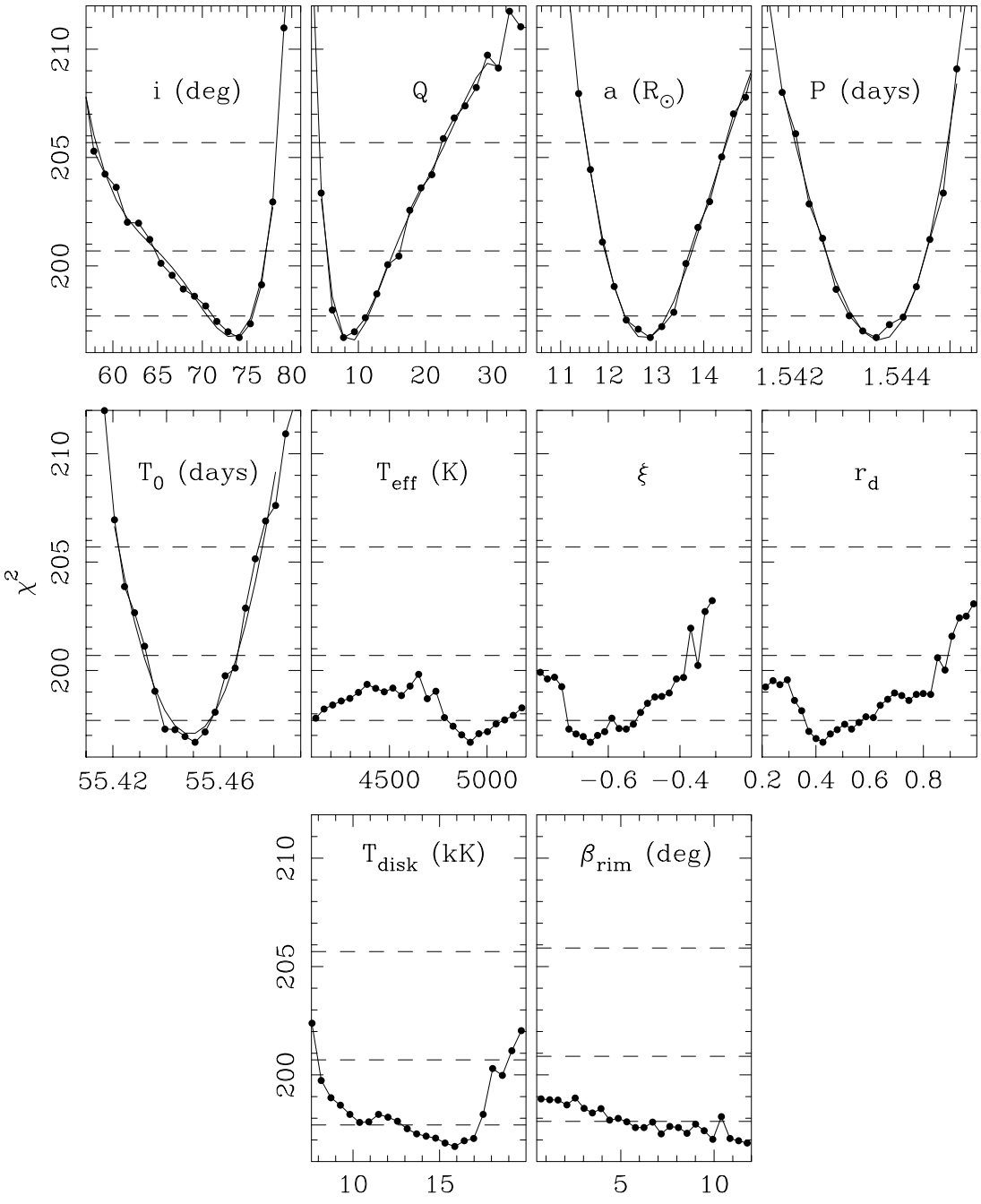

FIG. 9.—Similar to Fig. 8, but for the fitting run B (the one with $V_{\rm rot} \sin i = 90 \pm 10$ km s^{-1} as a fitting constraint)

the observed rotational velocity was not included in the total χ^2, the value of Q can only be assigned a lower limit ($Q > 6$ at the 3 σ level). However, the mass ratio Q does have well-defined upper and lower limits in the fitting run B, where the observed rotational velocity was included in the total χ^2. On the other hand, the accretion disk parameters and the effective temperature of the secondary star are not so well constrained.

Figure 10 shows the collapsed χ^2 function for six derived parameters in fitting run A: M_1 (the compact object's mass), and M_2 (the secondary star's mass), $V_{\rm rot} \sin i$, (the predicted rotational velocity of the secondary star), R_2 (the secondary star's radius), $\log g$ (the secondary star surface gravity), and L_2 (the secondary star's bolometric luminosity). Figure 11 shows the similar plot for fitting run B. Key results are summarized are in Table 3. The nominal mass of the black hole is 9.41 $M_\odot$ for fitting run A and 10.56 $M_\odot$ for fitting run B, respectively. We will adopt the results from fitting run B in the following discussions.

The only observational constraint related to the disk at present is that the disk should contribute roughly 30% of the light in the V band, and there is a wide range of accretion disk parameters that produce a disk with roughly the correct brightness. Since the inclination seems to be fairly high, the disk may partially eclipse the secondary star, and vice versa. Unfortunately, we do not have complete phase coverage, so we cannot at present detect the subtle signatures of grazing eclipses. Therefore, observations with much better phase

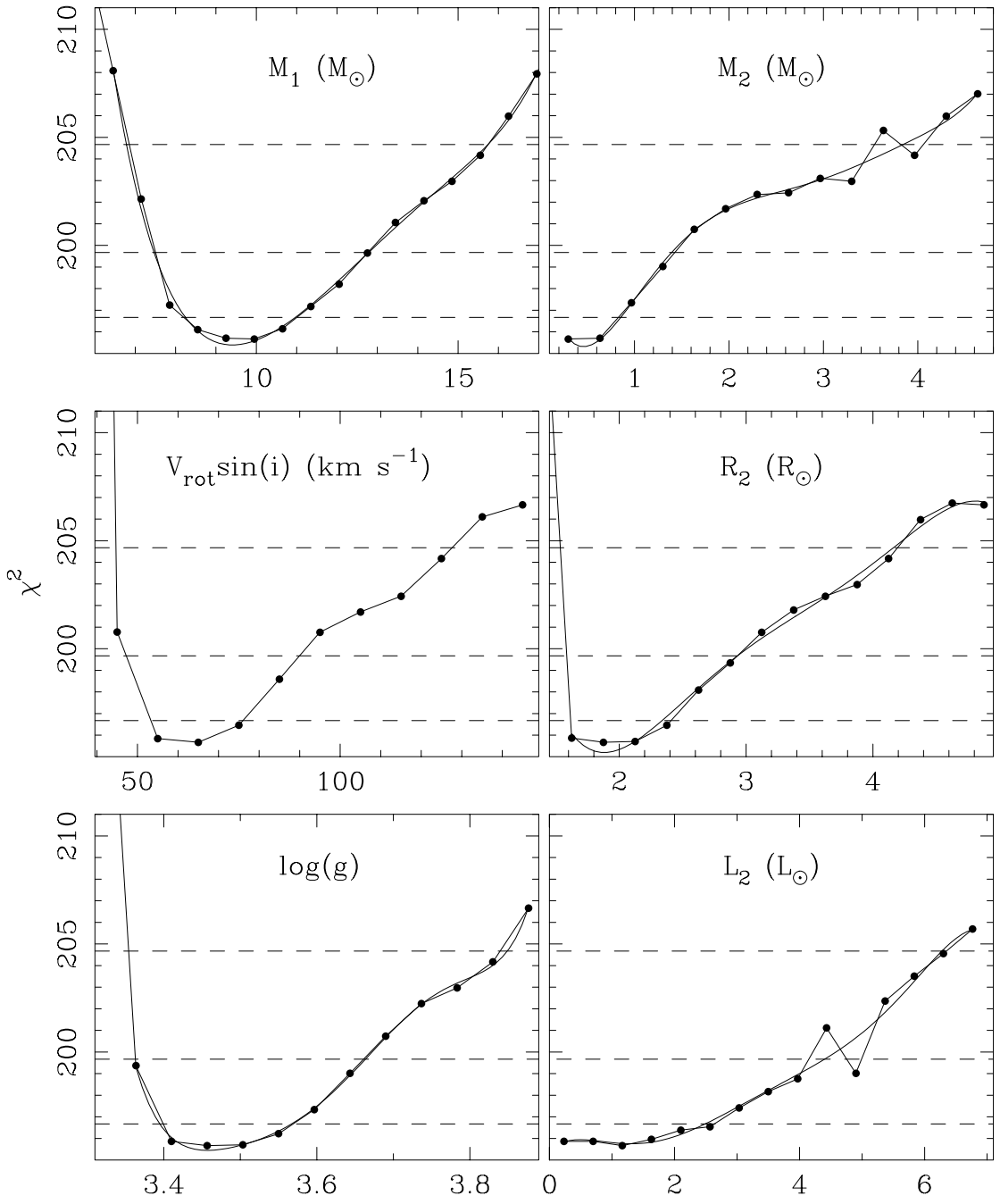

FIG. 10.—The χ^2 values as a function of various derived parameters for fitting run A (the run without a $V_{\rm rot} \sin i$ constraint). They are the black hole mass M_1 in solar masses, the secondary star mass M_2 in solar masses, the predicted projected rotational velocity of the secondary star $V_{\rm rot} \sin i$ in km s^{-1}, the radius of the secondary star R_2 in solar radii, the surface gravity of the secondary star $\log g$ in cgs units, and the bolometric luminosity of the secondary star L_2 in solar units. Fifth- or sixth-order polynomial fits to the curves used to get the confidence regions are shown as the smooth lines. The dashed lines denote the 1, 2, and 3 σ confidence limits.

coverage near the conjunction phases should be obtained. Alternatively, observations in the infrared (i.e., J, H, and K bands) would also be especially useful since the usual assumption is that the relative contribution of the accretion disk is much smaller at these wavelengths. This assumption can and should be tested with good quality infrared spectra. If the disk turns out to be faint in the infrared, then the model fits would of course be much less sensitive to the assumed disk parameters.

The inclusion of the rotational velocity as an additional fitting constraint resulted in only a modest ($\approx$10%) change in the derived mass of the black hole. This is because the black hole mass scales as $f(M)(1 + 1/Q)^2$, and the mass ratio Q is relatively large. On the other hand, the derived properties of the secondary star are quite different between the two fitting runs. For example, $M_2 < 0.79\ M_\odot$ (1 σ) for fitting run A and $M_2 = 1.31\ M_\odot$ for fitting run B. Clearly, a better measurement of $V_{\rm rot} \sin i$ would be quite useful since it would place a much stronger constraint on the mass ratio, which in turn would place stronger constraints on the properties of the secondary star. In order to significantly improve

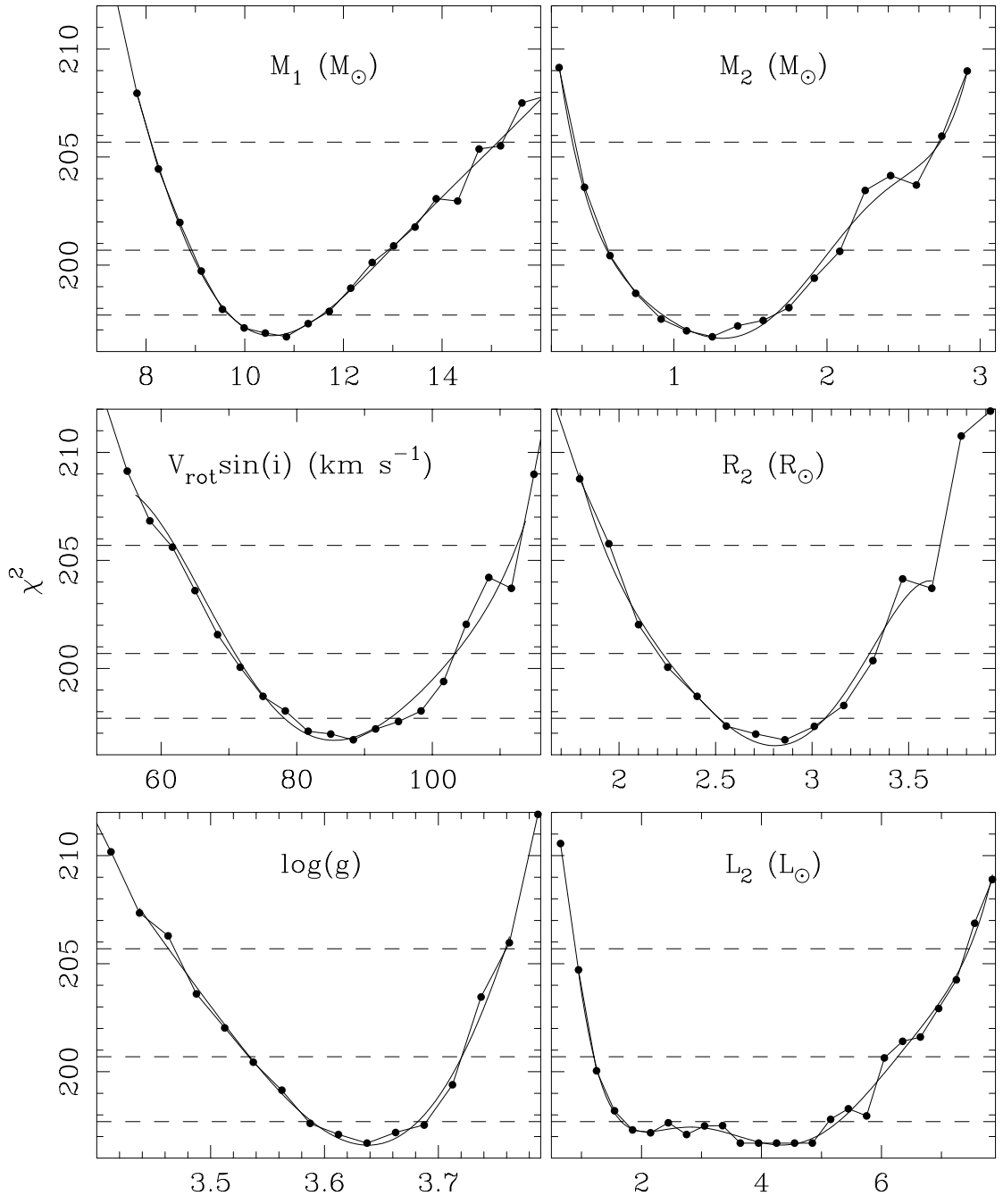

FIG. 11.—Similar to Fig. 10, but for fitting run B (the one with $V_{\rm rot} \sin i = 90 \pm 10$ km s^{-1} as a fitting constraint)

the precision of the black hole mass, one would need to also improve the precision of the mass function $f(M)$.

Finally, it is worthwhile to point out that the results summarized in Table 3 are our best estimates based on the data we currently have. Although the parameter uncertainties have been rigorously computed, they represent *statistical* errors only. There may be systematic errors in, for example, the measured rotational velocity $V_{\rm rot} \sin i$ owing to the low spectral resolution or in the derived inclination owing to the less than perfect phase coverage and errors in measuring the contamination from the accretion disk. It was straightforward to perform two fitting sequences to see what effect including the rotational velocity as a fitting constraint had on the outcome. It is less straightforward to quantify the effects of incomplete phase coverage or imperfect disk/stellar decomposition. However, we can say with some confidence that since our derived inclination is already quite high and near the upper limit imposed by the lack of X-ray eclipses, it is unlikely that we have underestimated the true inclination significantly. Ultimately one would need to obtain additional data to see if similar light curves are observed.

3.6. *Distance*

The distance to the source is a function of four parameters: The mass M_2 and temperature $T_{\rm eff}$ of the secondary star fix its luminosity (see eq. [2]); interstellar extinction (A_V) makes the source appear fainter; and extra light from the

TABLE 3
FITTED AND DERIVED ASTROPHYSICAL PARAMETERS FOR XTE J1550−564 FROM LIGHT-CURVE MODELING

	No $V_{\rm rot}\sin i$ Constraint			$V_{\rm rot}\sin i = 90 \pm 10$ km s^{-1}		
Parameter	Central Value	1 σ Range	3 σ Range	Central Value	1 σ Range	3 σ Range
Inclination (deg)	72.6	67.0–77.4	55.2–79.0	73.5	70.8–75.4	58.5–78.4
Mass ratio	≈21.0	> 12.0	> 3.6	8.5	6.7–11.0	4.5–22.5
Orbital separation ($R_\odot$)	11.96	11.52–12.50	10.79–15.09	12.77	12.35–13.22	11.53–14.45
Orbital period (days)	1.5435	1.5430–1.5440	1.5421–1.5449	1.5437	1.5432–1.5441	1.5421–1.5450
K_2 (km s^{-1})	359.4	350.2–368.6	331.2–387.4	361.2	352.3–370.1	333.8–388.2
Black hole mass ($M_\odot$)	9.41	8.36–10.76	6.81–15.60	10.56	9.68–11.58	8.10–15.15
Secondary star mass ($M_\odot$)	≈0.4	<0.79	<4.10	1.31	0.94–1.64	0.34–2.73
Total mass ($M_\odot$)	9.62	8.71–10.86	7.29–14.83	11.70	10.70–12.89	8.85–16.84
Secondary star radius ($R_\odot$)	≈1.88	1.62–2.24	1.63–4.06	2.81	2.55–3.04	1.93–3.61
Secondary star luminosity ($L_\odot$)	≈1.4	<2.5	<6.3	≈4.0	1.7–5.2	1.0–7.4
Secondary star gravity (log g)	3.46	3.40–3.56	3.36–3.84	3.63	3.59–3.68	3.46–3.76

accretion disk (parameterized by the V-band "disk fraction" k_V) makes the source appear brighter. We have reasonably good values for all of these parameters. As noted in § 3.3, $A_V \approx 4.75$ can be derived by modeling the X-ray spectrum and assuming a typical gas to dust ratio for the interstellar medium; $k_V \approx 0.30$ was determined from our spectral decomposition (Figs. 4*a* and 4*b*); and a temperature range of $4100 \leq T_{\rm eff} \leq 5100$ K was deduced for the secondary star. Using these results and a simple Monte Carlo procedure, we computed the distance and its uncertainty for various values of the secondary star mass M_2. We used the synthetic photometry computed from the NextGen models[6] to determine the expected absolute V magnitude of the star from its temperature, radius, and surface gravity. For this procedure we adopted $4100\ {\rm K} \leq T_{\rm eff} \leq 5100$ K, $k_V = 0.30 \pm 0.05$, a mean apparent V magnitude of 22.0 ± 0.2, $N_{\rm H} = (8.5 \pm 2.3) \times 10^{21}$ cm^{-2} (90% confidence), and $A_V = N_{\rm H}/1.79 \times 10^{21}$ (exact). The results are displayed in Table 4 for a wide range of secondary star masses. For masses in the range of 0.15–3.0 $M_\odot$ the computed distance is in the range 3.0–7.6 kpc. However, at a fixed mass, the formal error on the distance is rather large owing to the relatively large adopted temperature range and to the relatively large error in $N_{\rm H}$. The distance for the case of $M_2 = 1.31\ M_\odot$ is 5.9 kpc, again with a rather large formal error (1 σ range of 2.8 to 7.6 kpc).

We can make an independent estimate of the distance if we assume that the observed systemic velocity of $\gamma = -68 \pm 12$ km s^{-1} is entirely due to differential galactic rotation. We use the rotation curve of Fich, Blitz, & Stark (1989) and the standard IAU rotation constants of $R_0 = 8.5$ kpc and $\Theta_0 = 220$ km s^{-1}. The rotation curve for a source with Galactic coordinates of $l - 325\overset{\circ}{.}88$ and $b = -1\overset{\circ}{.}83$ is roughly parabolic, with a minimum radial velocity of ≈−95 km s^{-1} at a distance of ≈7 kpc. The expected distance for a source with $\gamma = -68$ km s^{-1} is either ≈4.4 or ≈9.7 kpc. Considering the errors on γ, the kinematic distance can be anywhere between ≈3.2 and ≈10.8 kpc at the 1 σ level, which is entirely consistent with the ranges derived above. Given the general agreement between the two distance estimates, we conclude that XTE J1550−564 has essentially no (radial) velocity with respect to its local standard of rest.

We can use the distance estimates for XTE J1550−564 to calculate an order of magnitude estimate for the maximum X-ray luminosity seen during outbursts. The spectral analysis of Sobczak et al. (2000) for the intense flare of 1998 September 19 implies an unabsorbed flux of 3.7×10^{-7} ergs cm^{-2} s^{-1} over the range of 1–20 keV, with the spectrum dominated by the power-law component. For our favored distance of 5.3 kpc, the isotropic luminosity is then 1.77×10^{39} ergs s^{-1} (with a large error owing to the uncertainty in the distance). This is just slightly above the Eddington luminosity for a 10.56 $M_\odot$ black hole, which is a remarkable coincidence given the significant uncertainty in the distance.

[6] See ftp://calvin.physast.uga.edu/pub/NextGen/Colors.

4. DISCUSSION

Bailyn et al. (1998) analyzed the distribution of black hole masses in seven systems and found a high probability that six of the seven systems (GRO J0422+32, A0620−00, GS 1124−683, GRO J1655−40, H1705−250, and GS 2000+25)

TABLE 4
DISTANCE AS A FUNCTION OF MASS

Assumed Secondary Mass ($M_\odot$)	Radius ($R_\odot$)	M_V for $T_{\rm eff} = 4600$ K	Distance for $T_{\rm eff} = 4600$ K (kpc)	1 σ Distance Range for $4100 \leq T_{\rm eff} \leq 5100$ K (kpc)
0.15	1.47	5.25	3.0	1.4–3.9
0.50	2.20	4.44	4.4	2.1–5.7
1.00	2.77	3.97	5.4	2.6–7.0
1.50	3.17	3.70	6.1	2.9–7.9
2.00	3.49	3.50	6.7	3.1–8.7
3.00	3.99	3.23	7.6	3.5–9.8

have masses which are consistent with $\approx 7\ M_\odot$. The seventh system, V404 Cyg, has a mass that is significantly larger (about 12 $M_\odot$; Shahbaz et al. 1994). The mass of the black hole in XTE J1550−564 is well above 7 $M_\odot$. With $M_1 \geq 8.1\ M_\odot$ at 3 σ confidence (Table 3), its mass may in fact be similar to the mass of the black hole in V404 Cyg. Since the work of Bailyn et al. (1998), the mass functions for seven additional systems have been measured, and improved parameters for some of the original seven systems have been measured. Thus the issue of the observed black hole mass distribution should be revisited to see if the clustering of black hole masses near 7 $M_\odot$ is still significant. Given the new data, we can begin to make meaningful comparisons with formation theory. For example, the detailed formation models of Fryer & Kalogera (2001) predict a mass distribution that is continuous and which extends over a broad range (in particular, they predict no peak at $\approx 7\ M_\odot$).

The determination of the black hole mass for XTE J1550−564 is especially important for the interpretation of the high-frequency X-ray QPOs observed for this system (Remillard et al. 2002; Homan et al. 2001). Models for several types of oscillations predicted in general relativity are under investigation as possible causes of these QPOs (e.g., Remillard 2001, and references therein); all of these depend on both the mass and spin of the black hole, and possibly also on conditions in the inner accretion disk. Despite considerable uncertainties in the models, we can offer a few comments on the implications of our mass determination for XTE J1550−564. At the nominal mass of 10.6 $M_\odot$, oscillations at the frequency of the last stable orbit for a Schwarzschild black hole (spin parameter, $a_* = 0$) would be seen at a frequency, $\nu = 2199/(M_{\rm BH}/M_\odot) = 208.2$ Hz (Shapiro & Teukolsky 1983). Since XTE J1550−564 has exhibited QPOs with frequencies up to 284 Hz (Homan et al. 2001), it appears that plausible mechanisms require $a_* > 0$. [The oscillation frequency would be 284 Hz (for $a_* = 0$) if $M_{\rm BH} = 7.74\ M_\odot$, which is below the 3 σ lower limit on the black hole mass.] This argument was used by Strohmayer (2001) to suggest that the 450 Hz QPO in GRO J1655−40 implies appreciable spin for the black hole in that system. We further note that the ratio of the black hole masses for XTE J1550−564 ($M_1 = 10.6\ M_\odot$; Table 3) and GRO J1655−40 ($M_1 = 6.3\ M_\odot$, Greene, Bailyn, & Orosz 2001) is ∼1.7, which is nearly inversely proportional to their maximum QPO frequencies: $(284/450\ {\rm Hz})^{-1} \sim 1.6$. We may then speculate that these results are consistent with a common QPO origin, with QPO frequencies that vary as M^{-1}, which might be expected if the black holes have similar values of the spin parameter.

Both XTE J1550−564 and GRO J1655−40 have had several closely spaced outburst events relatively shortly after their initial discoveries. Interestingly enough, optical precursors to X-ray outbursts (i.e., X-ray delays) have been observed for both sources. According to Hameury et al. (1997), these X-ray delays can best be understood using a two component accretion model consisting of a standard thin disk in the outer regions and an ADAF region in the inner region. At the onset of an outburst, the heating front reaches the ADAF region relatively quickly, but then must propagate more slowly on a viscous timescale, thereby greatly delaying the production of X-rays. Orosz et al. (1997) observed an optical precursor to the 1996 April outburst of GRO J1655−40. In that case, the delay between the *V*-band rise and the detection by the ASM on *RXTE* was 5.6 ± 0.8 days. In the case of the 2000 outburst of XTE J1550−564, Jain et al. (2001a) reported a delay of 8.8 ± 0.6 days between the rise in *V* and the detection by the *RXTE* ASM. The ratio of these delays is $8.8/5.6 \sim 1.6$, which is nearly the same as the ratio of the masses and is the same as the inverse ratio of their maximum QPO frequencies (∼1.7 and ∼1.6, respectively). We may again speculate that these results imply that the size of the ADAF cavity scales with the mass of the black hole.

For the case of a companion star mass of 1.3 $M_\odot$ (Table 3), the companion star in XTE J1550−564 appears to have mass that is larger than the typical mass for X-ray novae with a cool (K or M) companion. For comparison, the K0 secondary star in V404 Cyg has a mass of about 0.7 $M_\odot$ (Shahbaz et al. 1994). Since the secondary star in XTE J1550−564 is about 3 times larger than a normal K3/4 dwarf, its evolutionary state may be different than the dwarf secondaries in the short-period X-ray novae such as A0620−00 or GS 1124−683. If the star is still in the core hydrogen-burning phase, then its nuclear evolution timescale would be $\approx 1 \times 10^9$ yr, leading to an average mass-transfer rate of $10^{-9}\ M_\odot\ {\rm yr}^{-1}$. If the star has finished its core hydrogen burning, then presumably its radius is expanding on a thermal timescale of $\approx 10^7$ yr, leading to an average mass-transfer rate of $10^{-7}\ M_\odot\ {\rm yr}^{-1}$.

We can make a rough estimate of the mass-transfer rate in XTE J1550−564 as follows. The *RXTE* satellite performed numerous observations of XTE J1550−564 during its 1998 and 1999 outbursts. Sobczak et al. (2000) give the unabsorbed 2–20 keV flux and the 20–100 keV flux for the ≈200 PCA and the High-Energy X-Ray Timing Experient (HEXTE) observations from this period, respectively (their Fig. 6). Integrating under the curves, we find a total 2–100 keV fluence of 1.06 ergs cm^{-2} for the 1998–1999 outburst. Integrating the ASM light curve (Fig. 1), we find that the outburst in 2000 was about 20 times fainter in the 2–12 keV band than the 1998 and 1999 events. Assuming similar spectral characteristics for the two events, we conclude that total X-ray fluence in the 2–100 keV band was 1.1 ergs cm^{-2} in the interval between 1998 and 2001. To get the average mass-transfer rate, we need to know the recurrence time between major outbursts and the distance. According to Chen, Shrader, & Livio (1997), the sky coverage provided by scanning X-ray instruments has been quite good since about 1988, so it seems likely that the recurrence time of XTE J1550−564 is at least 10 yr. The distance is not well known, but it is probably about 6 kpc to within a factor of 2 (Table 4). In Table 5 we give total isotropic energies and average mass-transfer rates for assumed distances of 3, 6, and 10 kpc and recurrence times of 10 and 50 yr (we assume an accretion efficiency of 10% and that the mass-transfer rate from the secondary star is the same as the mass-transfer rate onto the black hole). The mass-transfer rates are between about 1×10^{-10} and $7 \times 10^{-9}\ M_\odot\ {\rm yr}^{-1}$, which suggests the star is evolving on a relatively long nuclear timescale.

GRO J1655−40 might be a similar system in terms of its evolutionary state. The average mass-transfer rate in GRO J1655−40 has been estimated to be about $1 \times 10^{-10}\ M_\odot\ {\rm yr}^{-1}$ (van Paradijs 1996). However, the secondary star is located in the Hertzsprung gap in the Hertzsprung-Russell diagram (e.g., Orosz & Bailyn 1997), so one would expect a mass-transfer rate of about $1 \times 10^{-7}\ M_\odot\ {\rm yr}^{-1}$ (e.g., Kolb

TABLE 5
TOTAL ENERGY AND MASS-TRANSFER RATE

Assumed Distance (kpc)	Assumed Recurrence Time (yr)	2–100 keV Fluence (erg)	Average Mass-Transfer Rate ($M_\odot$ yr^{-1})
3	10	1.1×10^{45}	6.0×10^{-10}
3	50	1.1×10^{45}	1.2×10^{-10}
6	10	4.3×10^{45}	2.4×10^{-9}
6	50	4.3×10^{45}	4.8×10^{-10}
10	10	1.2×10^{46}	6.7×10^{-9}
10	50	1.2×10^{46}	1.3×10^{-9}

et al. 1997). Regos, Tout, & Wickramasinghe (1998) have suggested that the secondary star in GRO J1655−40 is still in the core hydrogen-burning phase, and they have constructed evolutionary models with mass-transfer rates much closer to the observed value. It remains to be seen if a similar model can be constructed for XTE J1550−564.

Although the presence of a black hole in XTE J1550−564 is now firmly established, follow-up observations would be desirable to confirm and improve upon our results. The statistical error in the mass function can be easily reduced by adding more radial velocities. Spectroscopic observations with higher resolution should be obtained so that the rotational velocity of the companion star can be measured more precisely. Our inclination limits can be improved by obtaining multicolor light curves with much better phase coverage.

5. SUMMARY

Our optical spectroscopic observations of the companion star in XTE J1550−564 have established the orbital period of $P_{\rm sp} = 1.552 \pm 0.010$ days and the semiamplitude of $K_2 = 349 \pm 12$ km s^{-1}. The optical mass function is $f(M) = 6.86 \pm 0.71\ M_\odot$. The rotational velocity of the companion star is $V_{\rm rot} \sin i = 90 \pm 10$ km s^{-1}, which implies a mass ratio of $Q \equiv M_1/M_1 = 6.6^{+2.5}_{-1.6}$ (1 σ). This result should be confirmed with better data. From light-curve modeling we find the most likely value of the mass of the compact object is 9.41 $M_\odot$ with a 1 σ range of $8.36\ M_\odot \leq M_1 \leq 10.76\ M_\odot$. If we apply our tentative value of $V_{\rm rot} \sin i = 90 \pm 10$ km s^{-1} as an additional constraint in the ellipsoidal modeling, we find the most likely value of the mass of the compact object is 10.56 $M_\odot$ with a 1 σ range of $9.68\ M_\odot \leq M_1 \leq 11.58\ M_\odot$. The black hole nature of XTE J1550−564 is therefore firmly established by this work.

It is a great pleasure to thank the numerous people at the Las Campanas, Paranal, and La Silla Observatories who made this project a success, and the two YALO observers, Juan Espinoza and David Gonzalez Huerta, for providing data in a timely and efficient manner. J. A. O. appreciates useful discussions with Norbert Langer. C. D. B. and R. K. J. were supported in part by the NSF grant AST 97-30774, and J. E. M. was supported in part by NASA grant NAG 5-10813. P. J. G. was supported by a CfA Fellowship. R. R. acknowledges support from the NASA contract to MIT for instruments of the *RXTE* mission. This research has made use of the SIMBAD database, operated at CDS, Strasbourg, France, and NASA's Astrophysics Data System Abstract Service.

REFERENCES

Bailyn, C. D., Depoy, D., Agostinho, R., Mendez, R., Espinoza, J., & Gonzalez, D. 1999, BAAS, 195, 87.06
Bailyn, C. D., Jain, R. K., Coppi, P., & Orosz, J. A. 1998, ApJ, 499, 367
Bailyn, C. D., Orosz, J. A., McClintock, J. E., & Remillard, R. A. 1995, Nature, 378, 157
Bobinger, A. 2000, A&A, 357, 1170
Campbell-Wilson, D., McIntyre, V., Hunstead, R., & Green, A. 1998, IAU Circ. 7010
Cardelli, J. A., Clayton, G. C., Mathis, J. S. 1989, ApJ, 345, 245
Casares, J., Charles, P. A., & Marsh, T. R. 1995, MNRAS, 277, L45
Casares, J., Charles, P. A., & Naylor, T. 1992, Nature, 355, 614
Casares, J., Charles, P. A., Naylor, T., & Pavlenko, E. P. 1993, MNRAS, 265, 834
Charbonneau, P. 1995, ApJS, 101, 309
Chen, W., Shrader, C. R., & Livio, M. 1997, ApJ, 491, 312
Chitre, D. M., & Hartle, J. B. 1976, ApJ, 207, 592
Claret, A. 2000, A&A, 359, 289
Cui, W., Zhang, S. N., Chen, W., & Morgan, E. H. 1999, ApJ, 512, L43
Echevarría, J., Diego, F., Tapia, M., Costero, R., Ruiz, E., Salas, L., Gutiérez, L., & Enriquez, R. 1989, MNRAS, 240, 975
Fich, M., Blitz, L., & Stark, A. A. 1989, ApJ, 342, 227
Filippenko, A. V., & Chornock, R. 2001, IAU Circ. 7644
Filippenko, A. V., Leonard, D. C., Matheson, T., Li, W., Moran, E. C., & Riess, A. G. 1999, PASP, 111, 696
Filippenko, A. V., Matheson, T., & Barth, A. J. 1995, ApJ, 455, L139
Filippenko, A. V., Matheson, T., & Ho, L. C. 1995, ApJ, 455, 614
Fryer, C. L., & Kalogera, V. 2001, ApJ, 554, 548
Garcia, M. R., McClintock, J. E., Narayan, R., Callanan, P., Barret, D., & Murray, S. S. 2001, ApJ, 553, L47
Gotthelf, E., Halpern, J. P., Patterson, J., & Rich, R. M. 1992, AJ, 103, 219
Gray, D. F. 1992, The Observation and Analysis of Stellar Photospheres (Cambridge: Cambridge Univ. Press)
Greene, J., Bailyn, C. D., & Orosz, J. A. 2001, ApJ, 554, 1290
Greiner, J., Cuby, J. G., & McCaughrean, M. J. 2001, Nature, 414, 522
Hameury, J.-M., Lasota, J.-P., McClintock, J. E., & Narayan, R. 1997, ApJ, 489, 234
Hannikainen, D., Campbell-Wilson, D., Hunstead, R., McIntyre, V., Lovell, J., Reynolds, J., Tzioumis, T., & Wu, K. 2001, Ap&SS, 276, 45
Harlaftis, E. T., Steeghs, D., Horne, K., & Filippenko, A. V. 1997, AJ, 114, 117
Hauschildt, P. H., Allard, F., & Baron, E. 1999a, ApJ, 512, 377
Hauschildt, P. H., Allard, F., Ferguson, J., Baron, E., & Alexander, D. R. 1999b, ApJ, 525, 871
Homan, J., Wijnands, R., van der Klis, M., Belloni, T., van Paradijs, J., Klein-Wolt, M., Fender, R., & Méndez, M. 2001, ApJS, 132, 377
Horne, K., & Marsh, T. R. 1986, MNRAS, 218, 761
Horne, K., Wade, R. A., & Szkody, P. 1986, MNRAS, 219, 791
Jain, R. K., Bailyn, C. D., Orosz, J. A., McClintock, J. E., & Remillard, R. A. 2001a, ApJ, 554, L181
Jain, R. K., Bailyn, C. D., Orosz, J. A., McClintock, J. E., Sobczak, G. J., & Remillard, R. A. 2001b, ApJ, 546, 1086
Jain, R. K., Bailyn, C. D., Orosz, J. A., Remillard, R. A., & McClintock, J. E. 1999, ApJ, 517, L131
Jain, R., Bailyn, C., & Tomsick, J. 2001c, IAU Circ. 7575
Johnston, H. M., Kulkarni, S. R., & Oke, J. B. 1989, ApJ, 345, 492
Kalogera, V., & Baym, G. 1996, ApJ, 470, L61
Kolb, U., King, A. R., Ritter, H., & Frank, J. 1997, ApJ, 485, L33
Marsh, T. R., Robinson, E. L., & Wood, J. H. 1994, MNRAS, 266, 137
McClintock, J. E., Garcia, M. R., Caldwell, N., Falco, E. E., Garnavich, P. M., & Zhao, P. 2001, ApJ, 511, L147

McClintock, J. E., & Remillard, R. A. 1986, ApJ, 308, 110
Metcalfe, T. S. 2001, Ph.D. thesis, Univ. Texas
Mirabel, I. F., & Rodriquez, L. F. 1999, ARA&A, 37, 409
Narayan, R., McClintock, J. E., & Yi, I. 1996, ApJ, 457, 821
Orosz, J. A., & Bailyn, C. D. 1995, ApJ, 446, L59
———. 1997, ApJ, 477, 876
Orosz, J. A., Bailyn, C. D., Remillard, R. A., McClintock, J. E., & Foltz, C. B. 1994, ApJ, 436, 848
Orosz, J. A., & Hauschildt, P. H. 2000, A&A, 364, 265
Orosz, J. A., Jain, R. K., & Bailyn, C. D. 1998a, IAU Circ. 7009
Orosz, J. A., Jain, R. K., Bailyn, C. D., McClintock, J. E., & Remillard, R. A. 1998b, ApJ, 499, 375
Orosz, J. A., et al. 2001, ApJ, 555, 489
Orosz, J. A., Remillard, R. A., Bailyn, C. D., & McClintock, J. E. 1997, ApJ, 478, L83
Predehl, P., & Schmitt, J. H. M. M. 1995, A&A, 293, 889
Regos, E., Tout, C., & Wickramasinghe, D. 1998, ApJ, 509, 362
Remillard, R. A. 2001, in Evolution of Binary and Multiple Stars, ed. P. Podsiadlowski, S. Rappaport, A. King, F. D'Antona, & L. Burderi (San Francisco: ASP), in press (astro-ph/0103431)
Remillard, R. A., McClintock, J. E., & Bailyn, C. D. 1992, ApJ, 399, L145
Remillard, R. A., McClintock, J. E., Sobczak, G. J., Bailyn, R. A., Orosz, J. A., Morgan, E. H., & Levine, A. M. 1999, ApJ, 517, L127
Remillard, R. A., Muno, M. P., Sobczak, G. J., & McClintock, J. E. 2002, ApJ, in press
Remillard, R. A., Orosz, J. A., McClintock, J. E., & Bailyn, C. D. 1996, ApJ, 459, 226
Shahbaz, T., Ringwald, F. A., Bunn, J. C., Naylor, T., Charles, P. A., & Casares, J. 1994, MNRAS, 271, L10
Shapiro, S. L., & Teukolsky, S. L. 1983, Black Holes, White Dwarfs, and Neutron Stars (New York: Wiley)
Sobczak, G. J., McClintock, J. E., Remillard, R. A., Cui, W., Levine, A. M., Morgan, E. H., Orosz, J. A., & Bailyn, C. D. 2000, ApJ, 544, 993
Sobczak, G. J., McClintock, J. E., Remillard, R. A., Levine, A. M., Morgan, E. H., Bailyn, C. D., & Orosz, J. A. 1999b, ApJ, 517, L121
Smak, J. 1981, Acta Astron., 31, 395
Smith, D. A., et al. 1998, IAU Circ. 7008
Stetson, P. B., 1987, PASP, 99, 191
———. 1992a, in ASP Conf. Ser. 25, Astronomical Data Analysis Software and Systems I, ed. D. M. Worrall, C. Biemesderfer, & J. Barnes (San Francisco: ASP), 297
———. 1992b, in IAU Colloq. 136, Stellar Photometry—Current Techniques and Future Developments, ed. C. J. Butler & I. Elliot (Cambridge: Cambridge: Univ. Press), 291
Stetson, P. B., Davis, L. E., & Crabtree, D. R. 1991, in ASP Conf. Ser. 8, CCDs in Astronomy, ed. G. Jacoby (San Francisco: ASP), 282
Straižys, V., & Kuriliene, G. 1981, Ap&SS, 80, 353
Strohmayer, T. 2001, ApJ, 552, L49
Tomsick, J. A., Corbel, S., & Kaaret, P. 2001, ApJ, 563, 229
Tonry, J., & Davis, M. 1979, AJ, 84, 1511
van Paradijs, J. 1996, ApJ, 464, L139
Vrtilek, S. D., McClintock, J. E., Seward, F. D., Kahn, S. M., & Wargelin, B. J. 1991, ApJS, 76, 1127